A STUDY OF HEATING AND COOLING OF THE ISM IN NGC 1097 WITH *HERSCHEL*-PACS AND *SPITZER*-IRS[*]

P. Beirão[1], L. Armus[1], G. Helou[2], P. N. Appleton[3], J.-D. T. Smith[4], K. V. Croxall[4], E. J. Murphy[5], D. A. Dale[6], B. T. Draine[7], M. G. Wolfire[8], K. M. Sandstrom[9,22], G. Aniano[7], A. D. Bolatto[8], B. Groves[9], B. R. Brandl[10], E. Schinnerer[9], A. F. Crocker[11], J. L. Hinz[12], H.-W. Rix[9], R. C. Kennicutt[13], D. Calzetti[11], A. Gil de Paz[14], G. Dumas[9], M. Galametz[13], K. D. Gordon[15], C.-N. Hao[16], B. Johnson[17], J. Koda[18], O. Krause[9], T. van der Laan[9], A. K. Leroy[19,23], Y. Li[11], S. E. Meidt[9], J. D. Meyer[18], N. Rahman[8], H. Roussel[17], M. Sauvage[17], S. Srinivasan[17], L. Vigroux[20], F. Walter[9], and B. E. Warren[21]

[1] Spitzer Science Center, California Institute of Technology, Pasadena, CA 91125, USA; pedro@ipac.caltech.edu
[2] Infrared Processing and Analysis Center, California Institute of Technology, Pasadena, CA 91125, USA
[3] NASA Herschel Science Center, California Institute of Technology, Pasadena, CA 91125, USA
[4] Department of Physics and Astronomy, Mail Drop 111, University of Toledo, 2801 West Bancroft Street, Toledo, OH 43606, USA
[5] Carnegie Observatories, Pasadena, CA 91101, USA
[6] Department of Physics & Astronomy, University of Wyoming, Laramie, WY 82071, USA
[7] Department of Astrophysical Sciences, Princeton University, Princeton, NJ 08544, USA
[8] Department of Astronomy, University of Maryland, College Park, MD 20742, USA
[9] Max-Planck-Institut für Astronomie, Königstuhl 17, 69117 Heidelberg, Germany
[10] Leiden Observatory, Leiden University, P.O. Box 9513, 2300 RA Leiden, The Netherlands
[11] Department of Astronomy, University of Massachusetts, Amherst, MA 01003, USA
[12] Steward Observatory, University of Arizona, Tucson, AZ 85721, USA
[13] Institute of Astronomy, University of Cambridge, Madingley Road, Cambridge CB3 0HA, UK
[14] Departamento de Astrofisica, Facultad de Ciencias Fisicas, Universidad Complutense Madrid, Ciudad Universitaria, Madrid E-28040, Spain
[15] Space Telescope Science Institute, MD 21218, USA
[16] Tianjin Astrophysics Center, Tianjin Normal University, Tianjin 300387, China
[17] Institut d'Astrophysique de Paris, UMR7095 CNRS Université Pierre & Marie Curie, 98 bis boulevard Arago, 75014 Paris, France
[18] Department of Physics and Astronomy, SUNY Stony Brook, Stony Brook, NY 11794-3800, USA
[19] National Radio Astronomy Observatory, 520 Edgemont Road, Charlottesville, VA 22903, USA
[20] CEA/DSM/DAPNIA/Service d'Astrophysique, UMR AIM, CE Saclay, 91191 Gif sur Yvette Cedex, France
[21] ICRAR, M468, University of Western Australia, 35 Stirling Hwy, Crawley, WA 6009, Australia

ABSTRACT

NGC 1097 is a nearby Seyfert 1 galaxy with a bright circumnuclear starburst ring, a strong large-scale bar, and an active nucleus. We present a detailed study of the spatial variation of the far-infrared (FIR) [C II]158 μm and [O I]63 μm lines and mid-infrared H_2 emission lines as tracers of gas cooling, and of the polycyclic aromatic hydrocarbon (PAH) bands as tracers of the photoelectric heating, using *Herschel*-PACS and *Spitzer*-IRS infrared spectral maps. We focus on the nucleus and the ring, and two star-forming regions (Enuc N and Enuc S). We estimated a photoelectric gas heating efficiency ([C II]158 μm+[O I]63 μm)/PAH in the ring about 50% lower than in Enuc N and S. The average 11.3/7.7 μm PAH ratio is also lower in the ring, which may suggest a larger fraction of ionized PAHs, but no clear correlation with [C II]158 μm/PAH(5.5–14 μm) is found. PAHs in the ring are responsible for a factor of two more [C II]158 μm and [O I]63 μm emission per unit mass than PAHs in the Enuc S. spectral energy distribution (SED) modeling indicates that at most 25% of the FIR power in the ring and Enuc S can come from high-intensity photodissociation regions (PDRs), in which case $G_0 \sim 10^{2.3}$ and $n_H \sim 10^{3.5}$ cm^{-3} in the ring. For these values of G_0 and n_H, PDR models cannot reproduce the observed H_2 emission. Much of the H_2 emission in the starburst ring could come from warm regions in the diffuse interstellar medium that are heated by turbulent dissipation or shocks.

Key words: galaxies: individual (NGC 1097) – galaxies: ISM – galaxies: starburst – infrared: galaxies

Online-only material: color figures

1. INTRODUCTION

The most important heating process in the neutral interstellar medium (ISM) is expected to be the photoelectric effect working on polycyclic aromatic hydrocarbons (PAHs) and small dust grains (Watson 1972; Tielens & Hollenbach 1985; Wolfire et al. 1995; Hollenbach & Tielens 1999). Incident far-ultraviolet

photons have energies high enough to eject electrons from dust grains ($h\nu \gtrsim 6$ eV). They heat the gas via these photoelectrons, with a typical energy efficiency of 0.1%–1%. The efficiency is determined mostly by the ratio of UV radiation field to gas density (G_0/n) which sets the charge of the grains (Bakes & Tielens 1994; Weingartner & Draine 2001). The heated gas cools primarily via fine-structure lines such as [C II]158 μm and [O I]63 μm, with [C II]158 μm being dominant at lower densities and temperatures. The photoelectric effect on dust thus couples the far-ultraviolet radiation field to the interstellar gas heating outside of H II regions. Such regions where the dust photoelectric effect dominates gas heating and/or chemistry are

---

called photodissociation regions (PDRs; Hollenbach & Tielens 1999). Rotational transition lines of H_2 are also produced in PDRs, at the interface between the molecular gas and the atomic gas. The heating efficiency of the photoelectric effect is typically measured as the photoelectric yield per heating luminosity, using the flux ratio of the [C II]158 μm and/or [O I]63 μm to the far-infrared (FIR) luminosity. A further discussion on the definition of the photoelectric heating efficiency can be found in Section 4.2.

Observations of the FIR cooling lines in representative samples of local star-forming galaxies were pioneered with the Kuiper Airborne Observatory, but were first studied in local star-forming galaxies with the *Infrared Space Observatory* (*ISO*; Malhotra et al. 1997, 2001; Helou et al. 2001; Contursi et al. 2002). These studies clearly showed that the flux ratio [C II]158 μm/L(FIR) decreases by more than an order of magnitude (from 0.004 to less than 0.0004) for galaxies with high L(IR)/L(B) and/or warm dust temperatures while the [C II]158 μm/PAH ratios show no such trends with dust temperature or luminosity. This means that the role of PAHs on gas heating decreases with L(FIR)/L(B), which could be attributed to PAH ionization, or that [C II] becomes a less important cooling channel, resulting in more cooling via [O I]63 μm. In "active" regions with high FIR luminosity, [O I]63 μm becomes a more important cooling mechanism than [C II]158 μm (Malhotra et al. 2001). The mechanism responsible for heating these "active" regions is uncertain, but shock heating is one candidate, and energy injection from deeply embedded star formation in dense regions is another. Models of the integrated emission of [O I]63 μm, [C II]158 μm, H_2 vibrational modes, and other emission lines from Galactic and extragalactic star-forming regions have been used to diagnose these mechanisms (e.g., Hollenbach & McKee 1989; Kaufman et al. 2006). Unfortunately, the low spatial resolution of *ISO* at long wavelengths and the modest samples of sources detected in multiple lines make direct comparisons to models extremely difficult. With *Herschel*-PACS and *Spitzer*-IRS, there is now the opportunity to use the PAH bands and the main infrared cooling lines to study the variations of the photoelectric heating efficiency and diagnose the main heating mechanisms of the ISM in an environment with a wide range of ISM phases.

With *Herschel*/PACS (Poglitsch et al. 2010) we are now able to target the most important cooling lines of the warm ISM on physical scales much smaller than previously possible. The KINGFISH project (Key Insights on Nearby Galaxies: a Far-Infrared Survey with *Herschel*, PI: R. C. Kennicutt) is an open-time *Herschel* key program that aims to measure the heating and cooling of the gaseous and dust components of the ISM in a sample of 61 nearby galaxies with the PACS and SPIRE instruments. The FIR spectral range covered by PACS includes several of the most important cooling lines of the atomic and ionized gas, notably [C II] 158 μm, [O I] 63 μm, [O III] 88 μm, [N II] 122 μm, and [N II] 205 μm.

NGC 1097 is a Seyfert 1 galaxy with a bright starburst ring with a diameter of 2 kpc and a strong large-scale stellar bar (Gerin et al. 1988; Kohno et al. 2003; Hsieh et al. 2008) with a length of 15 kpc. This bar may be responsible for driving gas into the central region of the galaxy, forming a ring of gas near the Inner Lindblad Resonance, triggering the formation of massive star clusters (e.g., Athanassoula 1992). There is also gas inflow inside the ring possibly fueling the central supermassive black hole (Prieto et al. 2005; Fathi et al. 2006; Davies et al. 2009), triggering the formation of a compact star cluster seen near the nucleus. The star-forming ring and the nucleus of NGC 1097 are prominent in CO 1–0 (Kohno et al. 2003) as well as rovibrational H_2 and hydrogen recombination lines (Reunanen et al. 2002; Kotilainen et al. 2000). Tracers of denser molecular gas such as CO 2–1 and HCN (Kohno et al. 2003) peak at the nucleus and where the dust lanes and the ring intersect. A relatively bright, central concentration of the HCN emission also coincides with the nucleus, caused either by relatively dense molecular gas ($n \sim 10^5$ cm^{-3}) or by a strong X-ray radiation field from the nucleus that is affecting the chemistry (Meijerink et al. 2007).

Far-infrared photometry of NGC 1097 using PACS was first presented in Sandstrom et al. (2010), which showed that the ring dominates the FIR luminosity of the galaxy. Therefore, with PACS it is possible to isolate the ring contribution to FIR luminosity. Sandstrom et al. (2010) also showed that mid- and far-IR band ratios in the ring vary by less than ±20% azimuthally, indicating modest variation in the radiation field heating the dust on 600 pc scales. Sandstrom et al. (2010) provide a better estimate of the total bolometric emission arising from the active galactic nucleus (AGN) and its associated central starburst. The properties of the diffuse gas in the central ring have been investigated by Beirão et al. (2010) using the PACS spectrograph. They observed an enhancement of [O I] 63 μm/[C II] 158 μm ratio and [N II] 122 μm/[N II] 205 μm in the ring, which could correspond to an enhancement in the intensity of radiation field and density in the ring. Croxall et al. (2012) also include PACS observations of NGC 1097 to study general trends of the ISM heating and cooling. NGC 1097 is therefore an ideal system to study the physical conditions of the ISM in a nearby galaxy with both a starburst and an active nucleus. However, the FIR maps used in this study does not probe H II regions, nor the warm molecular gas, which can trace shock and AGN excitation, nor do they compare the *Herschel* data to the emission in the mid-infrared where the strong PAH features reside. These ISM phases are better studied using emission lines found in the mid-infrared (5–40 μm).

In this paper we present a study of the properties of the heating and cooling processes of the ISM in the ring and bar of NGC 1097 based on spectral maps using PACS on board the *Herschel Space Observatory* and the Infrared Spectrograph (IRS) on board the *Spitzer Space Telescope*. These two instruments are necessary to cover the wavelength range from 5.5–230 μm, where the most important tracers of gas heating and cooling are emitted. We will diagnose ISM properties such as PAH ionization and heating efficiency to answer the following questions: how does the gas heating efficiency vary with PAH ionization? Is there a variation of PAH heating efficiency between the ring and the regions at the bar? Is the mechanical energy created by the inflow of gas into the ring an important component of the gas heating in the ring? In this paper we address these issues in the following sections: in Section 2 we present the observations and describe the reduction process of the *Spitzer*-IRS data into data cubes; in Section 3 we present the spectra and the spectral maps of the nucleus and both ends of the bar for several spectral features such as PAHs and H_2 lines and use ratio maps to analyze the PAH emission distribution, the gas heating efficiency, and the cause of the warm H_2 emission; in Section 4 we discuss the implications of the results in Section 3. Our main conclusions are summarized in Section 5. Throughout the paper we use a distance of 19.1 Mpc for a cosmology $H_0 = 75$ km s^{-1} Mpc^{-1}, using the Tully–Fisher relation (Willick et al. 1997).

Table 1
Exposure Times

| Region	SL (5.5–14.5 μm)	LL (14–38 μm)	SH (10.5–19.5 μm)	LH (19–38 μm)
Nucleus and ring	2196 s	2139 s	6696 s	930 s
Enuc N	3294 s	. . .	5544 s	2684 s
Enuc S	3294 s	. . .	6804 s	2684 s

2. OBSERVATIONS AND DATA REDUCTION

NGC 1097 was a Science Demonstration Phase target observed with the *Herschel*-PACS instrument as part of the KINGFISH open-time program. The galaxy was observed with the PACS integral field unit in both chop-nod and wavelength-switching modes. The observations and data reduction procedure of the PACS spectroscopy data were described in Beirão et al. (2010). The observations use a 2×2 oversampled raster map strategy (step size 12″). The standard pipeline procedure for this, and part of the HIPE chop-nod pipeline, is to grid these four separate observations onto a common R.A.–decl. grid using a smaller pixel scale than the native $9\rlap.{''}4 \times 9\rlap.{''}4$ pixels size (in this case $3'' \times 3''$ sub-pixels). For updates on PACS reduction and a discussion on the differences between observations in chop-nod and wavelength-switching mode, see Croxall et al. (2012), which also studies general trends of the ISM heating and cooling.

NGC 1097 was observed with *Spitzer*-IRS in spectral mapping mode as part of the Spitzer Infrared Nearby Galaxy Survey (SINGS; Kennicutt et al. 2003), under program ID 159. The central region which includes the ring and the nucleus was observed using all high- and low-resolution modules, and the edges of the large-scale bar, which we refer to as the northern and southern extranuclear regions (Enuc N and S), was observed using all high-resolution modules but with only SL (5–14 μm) at low resolution. The central region was observed on 2004 July 18, and the Enuc N and S regions were observed on 2005 August 8. Table 1 summarizes all the observations. In Figure 1 we show all the footprints of the IRS observations performed on NGC 1097. We extracted only the maps that contain both modules SL1 and SL2 or LL1 and LL2. While the short–low (SL) module was oriented in a parallel direction relative to the bar, the long–low (LL) module was oriented in a perpendicular direction relative to the bar. The high-resolution modules, short–high (SH) and long–high (LH), were oriented at an angle of 45° relative to the bar. *Spitzer*-IRS spectra of the central region of NGC 1097 have been published before by Brandl et al. (2006) and the *Spitzer*-IRS observations of the nuclear regions for all SINGS galaxies including NGC 1097 are described in Smith et al. (2007b; low-resolution spectra) and Dale et al. (2009; high-resolution spectra). However, these measurements were averaged over large areas. Here we publish the complete IRS spectral maps of NGC 1097 for the first time. The total exposure times are given in Table 1.

We used CUBISM (Smith et al. 2007a) to build SL and LL spectral cubes from sets of mapping mode basic calibrated data (BCD) observations taken with *Spitzer*-IRS. In order to create continuum-subtracted maps of spectral lines and PAH features, we use PAHFIT (Smith et al. 2007b). PAHFIT is a spectral fitting routine that decomposes IRS low-resolution spectra into broad PAH features, unresolved line emission, and continuum emission from dust grains. PAHFIT allows for the deblending of overlapping features, in particular the PAH emission, silicate
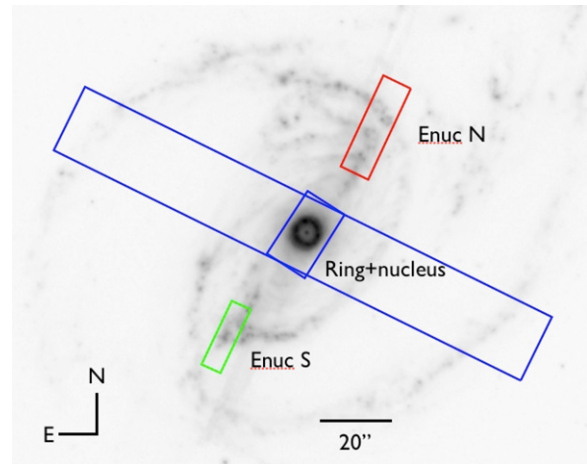
Figure 1. Footprints of the *Spitzer*/IRS spectral maps of NGC 1097, overlaid on an IRAC 8 μm image from the SINGS program (ID 159). The labels refer to the Ring+nucleus (blue), Enuc N (northern edge of the bar, in red), and Enuc S (southern edge of the bar, in green), analyzed in this paper. The Enuc N and Enuc S regions have only short–low observations, while the ring+nucleus have spatial coverage of the IRS with short–low and long–low IRS modules.
(A color version of this figure is available in the online journal.)

absorption, and fine-structure lines. This is not possible using CUBISM. Because it performs a simultaneous fit to the emission features and the underlying continuum, PAHFIT works best if it can fit combined SL and LL spectra across the full 5–40 μm range for which it was intended. In order to provide a stable long-wavelength continuum from which to estimate the true PAH emission, including the broad feature wings, we formed a combined SL + LL cube by rotating and re-gridding the LL cubes to match the orientation and pixel size of the SL cubes ($1\rlap.{''}85 \times 1\rlap.{''}85$). By calculating the flux in the new LL cubes using a bilinear interpolation (in surface brightness units), we assure that the flux over the native LL pixel scale is conserved. Finally, a small average-scale factor of 0.81, calculated by comparing pixels in the spectral overlap region between SL and LL at approximately 14 μm, is applied to the SL data before running PAHFIT on the combined SL + LL cubes. The output of PAHFIT is saved for each feature, and is used to create the PAH feature maps at the native resolution of the SL data as shown in Figure 3. All subsequent comparisons of the PAH emission with the PACS data are derived from the SL and LL cubes smoothed to the resolution of the relevant PACS features, as described in the text, and not from the high-resolution PAH images shown in Figure 3. We also used CUBISM to build SH and LH cubes from sets of mapping mode BCD observations and to make maps of [S III]18.7 μm, [S III]33.5 μm, and [Si II]34.5 μm.

We also used *Spitzer*-IRAC 8 μm and *Spitzer*-MIPS 24 μm images of NGC 1097, observed as a part of SINGS (for a complete description see Dale et al. 2005). The 8 μm map was corrected for stellar light using a scaled 3.6 μm image following Helou et al. (2004).

3. RESULTS AND ANALYSIS

3.1. Spectra

In Figure 2 we present the average low-resolution spectra of the four regions highlighted in this study (ring (blue), Enuc N (red), and Enuc S (green)) and a small region centered in the nucleus (in gray). These spectra were produced by extracting a rectangular area from each spectral cube using CUBISM:
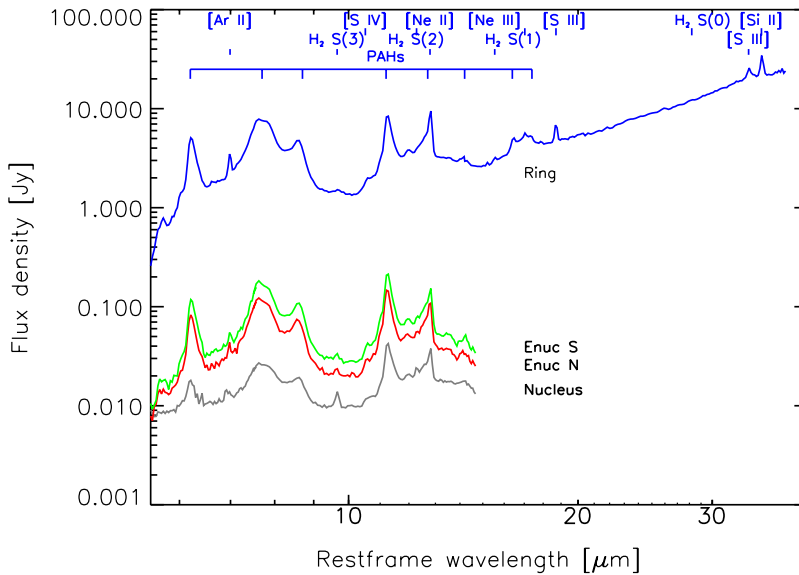
Figure 2. *Spitzer*/IRS low-resolution spectra of the ring (blue), Enuc N (red), and Enuc S (green), and the nucleus (gray). All low-resolution spectra include the SL wavelength range (5–14 μm) but only the ring includes IRS LL (14–38 μm). The Enuc N and Enuc S regions were not observed in LL. The labels indicate the positions of the main spectral features in the mid-infrared.

(A color version of this figure is available in the online journal.)

$17'' \times 17''$ for the ring and $3''.7 \times 3''.7$ for the nucleus. For Enuc N, the areas are $24''.1 \times 40''.7$ and for Enuc S, the areas are $16''.7 \times 37''$. The spectrum of the ring is the only one that covers the full 5–38 μm range sampled by the SL and LL data. The nuclear spectrum has been subtracted from the ring spectrum in Figure 2 to avoid contamination from the central AGN. Our low-resolution spectra are very similar and show the typical characteristics of star-forming regions: prominent PAH features, a possible absorption feature at 9.7 μm, and a continuum that rises with wavelength. To make a quantitative comparison between these regions, we used PAHFIT to decompose the low-resolution spectra. We measured the flux of the PAH features, ionic lines, and H_2 lines, and the results are listed in Tables 2 and 3. One of the most prominent differences between the nuclear region and the ring is the flux of the H_2 lines at 9.7 μm and 12.3 μm compared to the PAH features. The flux ratio $H_2 S(3)/PAH 7.7 \mu$m is $\sim$0.009 in the nucleus but only $\sim$0.004 in the ring and $\sim$0.001 in the Enuc regions.

3.2. PAH Emission Distribution

PAHs constitute between 10% and 20% of the interstellar carbon, and were first identified as a possible carrier of the wide emission features at 6.2, 7.7, 8.6, 11.3, and 12.7 μm by Leger & Puget (1984) and Allamandola et al. (1985). These bands are emitted by PAH molecules following photoexcitation. The same PAHs dominate the photoelectric heating of the diffuse ISM. Ionized PAHs are usually associated with the emission bands at 6.2, 7.7, 8.6 μm, whereas neutral PAHs are responsible for the emission bands at 11.3 and 12.7 μm. The larger PAHs emit at longer wavelengths (e.g., Allamandola et al. 1999; Hony et al. 2001). For this reason the PAH ratios 11.3/7.7 μm can be used to diagnose PAH ionization, and 6.2/7.7 μm can be used to diagnose grain size (e.g., Draine & Li 2001), although with caveats, as the 11.3/7.7 μm also varies slightly with size.

In Figure 3 we present spectral maps of the continuum-subtracted total PAH emission between 5 and 14 μm for the ring, the northern end of the bar (Enuc N), and the southern end of the bar (Enuc S). Each map was constructed by smoothing

the 6.2, 7.7, 8.6, 11.3, and 12.7 μm to the 14 μm resolution, assuming that the point spread function (PSF) at 14 μm can be approximated to a Gaussian with FWHM $\sim 4''.1$. The map of the ring reveals that the average PAH surface brightness in the ring is a factor of 10 higher than in the nucleus and outer regions. The PAH surface brightness varies by a factor of $\sim$4 throughout the ring, and peaks in a hotspot north of the nucleus. This is the same hotspot where a maximum of [O I]63 μm/[C II]158 μm was also observed by Beirão et al. (2010), which was interpreted as a region with an intense radiation field. PAH flux in the nucleus is a factor of $\sim$10 lower than in the ring, but as seen in Figure 2 is still quite strong. We can compare this result to other studies that involve PAH observations in the nucleus on NGC 1097 at a higher spatial resolution. Mason et al. (2007) found no PAH 3.3 μm in the central $0''.2$, but they do find strong PAH 11.3 μm emission over a $3''.6$ region. As seen in Figure 2 we also observe strong PAH emission in the nucleus over a similar area, so our results are in agreement. In the Enuc N and S, the PAH surface brightness varies by a factor of $\sim$10, peaking near star-forming regions.

In Figure 4 we show spectral maps of the 11.3/7.7 μm PAH ratios of the ring and extranuclear regions at both ends of the bar. These maps were produced using 7.7 μm and 11.3 μm PAH maps smoothed to a $4''.1$ resolution using a Gaussian kernel. The ratio increases up to a factor of two from a low of $\sim$0.2 in the ring to a peak of $\sim$0.4 outside of the ring and in the nucleus. In the extranuclear regions the ratio varies in the same proportion, with the lowest ratio coinciding with the star-forming regions. However, in Enuc N the PAH surface brightness peak at the southern end of the map does not coincide spatially with a low value of 11.3/7.7 μm PAH ratio. This is surprising, but the reason is not clear, and indicates that the PAH ratios are not always a direct indicator of the starlight intensity. In Figure 5 we plot the 11.3/7.7 μm PAH ratio as a function of 6.2/7.7 μm using PAH 6.2, 7.7, and 11.3 maps for the ring (blue), Enuc N (red), and Enuc S (green). These maps were convolved to the resolution at 11.3 μm, $2''.7$, assuming a Gaussian PSF. Each point corresponds to a $3''.7 \times 3''.7$ region. The tracks indicate 6.2/7.7 μm and 11.3/7.7 μm
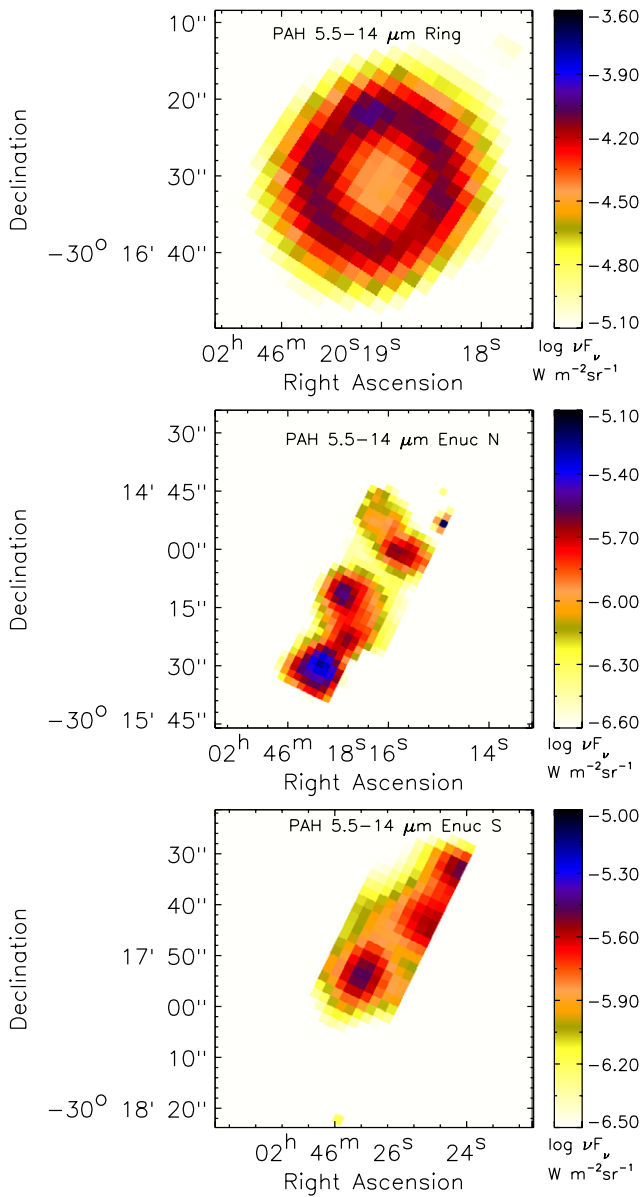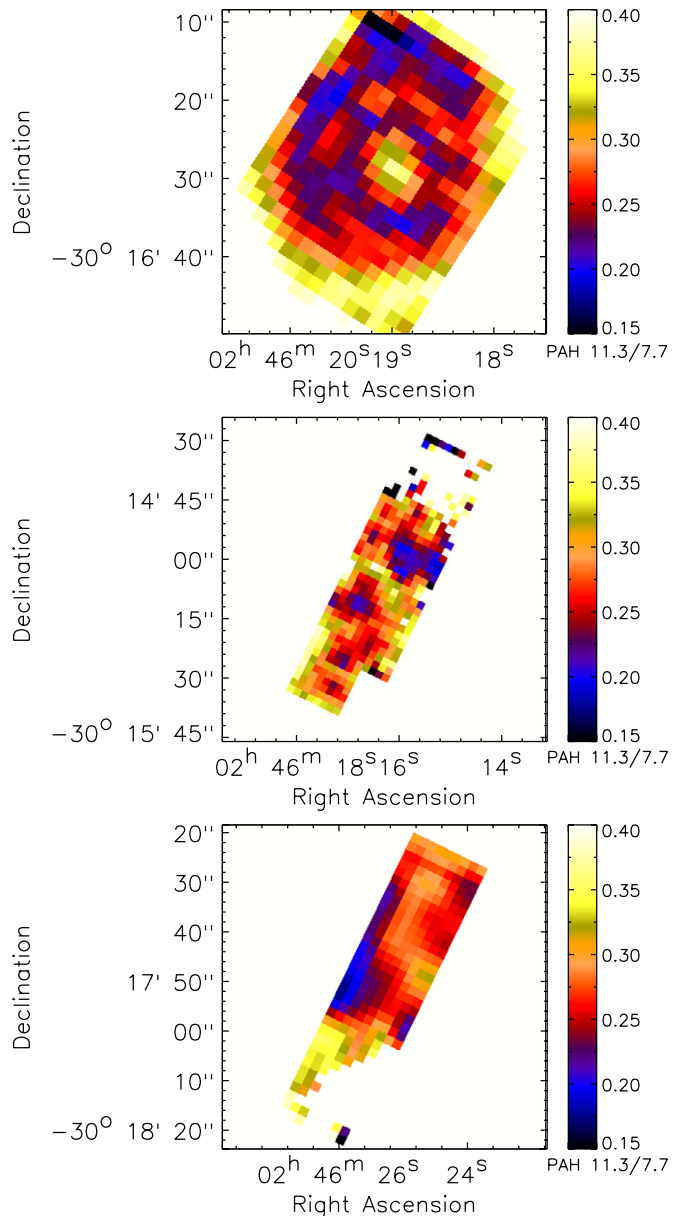
Figure 3. Maps of the total PAH emission between 5 and 14 μm in the ring and nucleus (upper), Enuc N (center), and Enuc S (lower). Each image has a resolution matched to the IRS PSF at 14 μm which we approximate as a 4''.1 FWHM Gaussian. The pixel scale is 1''.85 pixel^{-1}. North is up.

(A color version of this figure is available in the online journal.)

Figure 4. Emission maps of the 11.3/7.7 μm PAH ratio in the ring and nucleus (upper), Enuc N (center), and Enuc S (lower). Each image has a resolution matched to the IRS PSF at 14 μm which we approximate as a 4''.1 FWHM Gaussian. The pixel scale is 1''.85 pixel^{-1}. North is up.

(A color version of this figure is available in the online journal.)

PAH ratios for neutral and ionized PAH grains (Draine & Li 2001), and the dot-dashed line indicates where PAH grains have approximately 250 C atoms. The error bars indicate representative measurement uncertainties. The 11.3/7.7 μm values for the ring are concentrated at ~0.23, but there is a wider dispersion for the Enucs. The 6.2/7.7 μm ratio is on average 20% larger in the Enuc N and S than in the ring, but 20% lower in the nucleus than in the ring. This suggests that on average PAH grains may be smaller in the Enuc regions, but larger in the nucleus than in the ring. Table 2 shows the integrated fluxes of the main PAH features and PAH ratios in the ring, nucleus, Enuc N, and Enuc S.

3.3. Fine-structure Lines and PAH Emission

For a direct comparison between the PACS and the IRS data, we measured the flux of the [C II]158 μm and [O I]63 μm

fine-structure lines, the total flux of the PAH emission features between 5.5 and 14 μm, the 11.3/7.7 μm PAH ratio, and the 70 μm/100 μm ratio in the ring and extranuclear positions over a grid composed of 12'' × 12'' square regions, shown in Figure 6. We chose these regions to properly sample the flux at the longest wavelength where the FWHM is close to 11''. Before measuring the total PAH flux and the 11.3/7.7 μm PAH ratio, we made convolution kernels to smooth each PAH feature map at 6.2, 7.7, 8.6, 11.3, 12.6, and 14.1 μm to the *Herschel* beam at 160 μm, using PSFs calculated by Aniano et al. (2011), and theoretical PSFs for IRS made with STinyTim for each wavelength above. We then rebinned all maps to match the pixel size used in the PACS FIR spectral maps (3'' pixel^{-1}). The PAH 7.7 μm and the 11.3 μm fluxes were measured summing all pixels within each region in Figure 6. We also used

Table 2
Emission Line Fluxes from *Spitzer*-IRS

Region	Aperture Size (arcsec²)	PAH 6.2 μm	[Ar II] 6.99 μm 15.8 eV	PAH 7.7 μm	PAH 8.6 μm	[Ar III] 8.99 μm 27.6 eV	[S IV] 10.5 μm 34.8 eV	PAH 11.3 μm	PAH 12.6 μm	[Ne II] 12.8 μm 21.6 eV	[Ne III] 15.6 μm 41.0 eV	[S III] 18.7 μm 23.3 eV	[S III] 33.5 μm 23.3 eV	[Si II] 34.8 μm 8.2 eV	PAH Total 6.2–12.6 μm	PAH Ratio 11.3/7.7	PAH Ratio 6.2/7.7
Nucleus	96.8	2.44 ±0.19	0.103 ±0.025	11.2 ±0.6	1.93 ±0.12	. . . . . .	0.275 ±0.003	3.69 ±0.07	2.34 ±0.07	0.364 ±0.004	0.415 ±0.050	0.136 ±0.001	0.246 ±0.003	0.576 ±0.003	21.6 . . .	0.33 . . .	0.23 . . .
Ring	680.1	32.6 ±1.3	1.726 ±3.68	130.4 ±4.6	23.3 ±1.0	0.518 ±0.013	0.206 ±0.008	30.5 ±0.5	20.3 ±0.7	4.59 ±0.01	0.205 ±0.003	1.18 ±0.01	1.72 ±0.01	3.81 ±0.01	237.1	0.23	0.25
Enuc N	1067.2	1.68 ±0.09	0.048 ±0.009	5.79 ±0.08	. . . . . .	0.009 ±0.002	1.03 ±0.15	1.32 ±0.11	0.129 ±0.002	. . . . . .	. . . . . .	. . . . . .	. . . . . .	. . . . . .	10.5	0.23	0.29
Enuc S	739.3	1.59 ±0.09	0.074 ±0.002	5.26 ±0.07	1.06 ±0.17	. . . . . .	. . . . . .	1.32 ±0.10	0.66 ±0.06	0.178 ±0.35	. . . . . .	. . . . . .	. . . . . .	. . . . . .	9.89 . . .	0.25	0.30

Note. In Units of 10^{-17} W m^{-2}.

Table 3
H$_2$ Line Fluxes[a] from Low- and High-resolution Spectra

Region	Area (arcsec^2)	$S(0)28.2\,\mu$m	$S(1)17.0\,\mu$m	$S(2)12.3\,\mu$m	$S(3)9.7\,\mu$m
Nucleus	96.8	0.55 ± 0.13	6.13 ± 0.78	6.21 ± 0.79	10.1 ± 1.01
Ring	680.1	10.7 ± 0.79	35.9 ± 1.2	20.7 ± 1.4	58.5 ± 16.1
Ring 1	96.8	0.77 ± 0.28	4.00 ± 0.63	6.13 ± 0.78	11.7 ± 1.1
Ring 2	96.8	1.96 ± 0.44	4.26 ± 0.65	4.53 ± 0.67	4.66 ± 0.68
Ring 3	96.8	0.99 ± 0.31	4.44 ± 0.67	5.86 ± 0.77	7.17 ± 0.85
Enuc N[b]	1067.2	0.209 ± 0.039	. . .	0.04 ± 0.01	0.561 ± 0.010
Enuc S[b]	739.3	0.322 ± 0.074	. . .	. . .	0.770 ± 0.015

Notes.
[a] In units of 10^{-17} W m^{-2}.
[b] From high-resolution spectra.

Table 4
PAH Band and Line Fluxes[a] for Each 12″ Region

Regions	PAH 7.7 μm	PAH 11.3 μm	PAH 6.2–12.6 μm	[S III]18.7 μm[b]	[S III]33.5 μm[b]	[Si II]34.8 μm[b]	[O I]63 μm	[C II]158 μm	FIR[c]
				Ring					
1	177 ± 8	42.9 ± 0.7	366 ± 7	2.02 ± 0.09	4.15 ± 0.01	7.19 ± 0.02	4.38 ± 0.45	9.91 ± 0.03	2280
2	256 ± 9	63.9 ± 1.0	545 ± 5	2.61 ± 0.10	4.50 ± 0.01	8.52 ± 0.02	7.37 ± 0.21	17.4 ± 0.1	3363
3	195 ± 6	50.0 ± 1.0	423 ± 6	2.01 ± 0.11	3.95 ± 0.01	7.46 ± 0.02	6.06 ± 0.18	14.2 ± 0.1	2467
4	244 ± 7	59.7 ± 1.1	514 ± 7	2.22 ± 0.10	4.34 ± 0.01	8.23 ± 0.02	5.44 ± 0.45	15.3 ± 0.1	3174
5	235 ± 7	60.6 ± 1.0	508 ± 7	2.30 ± 0.10	4.00 ± 0.01	8.30 ± 0.02	6.64 ± 0.35	17.4 ± 0.1	3317
6	171 ± 5	43.7 ± 0.8	358 ± 6	1.45 ± 0.14	3.00 ± 0.01	6.88 ± 0.01	3.46 ± 0.27	12.6 ± 0.1	2215
7	226 ± 8	57.3 ± 1.1	474 ± 9	1.92 ± 0.13	3.63 ± 0.01	7.99 ± 0.02	5.49 ± 0.55	17.5 ± 0.1	3101
8	172 ± 8	44.1 ± 0.8	360 ± 6	1.68 ± 0.13	3.05 ± 0.01	7.14 ± 0.02	4.42 ± 0.45	12.8 ± 0.1	2318
				Enuc N					
1	7.30 ± 0.35	2.02 ± 0.05	15.9 ± 0.3	0.359 ± 0.007	0.672 ± 0.107	0.629 ± 0.038	. . .	0.920 ± 0.046	71.4
2	6.73 ± 0.43	1.92 ± 0.05	14.7 ± 0.3	0.291 ± 0.006	0.642 ± 0.102	0.601 ± 0.036	. . .	0.712 ± 0.035	56.9
3	7.40 ± 0.38	2.16 ± 0.06	15.1 ± 0.3	0.221 ± 0.005	0.526 ± 0.084	0.486 ± 0.015	. . .	0.801 ± 0.040	75.4
4	7.54 ± 0.39	2.05 ± 0.04	17.0 ± 0.4	0.232 ± 0.005	0.703 ± 0.111	0.655 ± 0.039	. . .	0.889 ± 0.044	71.0
5	6.71 ± 0.52	1.73 ± 0.06	15.7 ± 0.4	0.117 ± 0.003	0.573 ± 0.091	0.535 ± 0.017	. . .	0.749 ± 0.037	56.9
6	9.75 ± 0.28	2.94 ± 0.05	22.0 ± 0.3	. . .	0.613 ± 0.018	0.656 ± 0.104	. . .	1.01 ± 0.05	91.3
7	6.99 ± 0.45	2.05 ± 0.06	16.2 ± 0.4	. . .	0.541 ± 0.032	0.582 ± 0.093	. . .	0.819 ± 0.040	71.2
8	8.43 ± 0.56	3.01 ± 0.06	18.2 ± 0.3	. . .	. . .	. . .	. . .	0.936 ± 0.042	103
9	8.86 ± 0.56	2.86 ± 0.06	21.2 ± 0.4	. . .	0.713 ± 0.113	0.671 ± 0.040	. . .	1.11 ± 0.05	97.3
10	5.32 ± 0.69	1.67 ± 0.09	13.4 ± 0.3	. . .	0.458 ± 0.073	0.427 ± 0.026	. . .	0.676 ± 0.033	54.1
				Enuc S					
1	8.96 ± 0.48	2.65 ± 0.04	20.7 ± 0.4	. . .	. . .	. . .	0.360 ± 0.102	1.12 ± 0.03	118
2	10.4 ± 0.5	2.82 ± 0.04	23.7 ± 0.4	. . .	0.068 ± 0.01	0.315 ± 0.09	0.356 ± 0.046	1.31 ± 0.01	104
3	11.6 ± 0.5	3.18 ± 0.04	26.5 ± 0.3	. . .	. . .	. . .	0.512 ± 0.058	1.86 ± 0.02	148
4	10.3 ± 0.5	2.60 ± 0.04	23.0 ± 0.3	0.058 ± 0.024	0.071 ± 0.023	0.229 ± 0.071	0.232 ± 0.036	1.10 ± 0.01	78.2
5	13.0 ± 0.6	3.24 ± 0.04	28.8 ± 0.3	0.068 ± 0.032	0.110 ± 0.032	0.436 ± 0.131	0.364 ± 0.036	1.74 ± 0.01	122
6	5.45 ± 0.51	1.50 ± 0.05	12.7 ± 0.5	. . .	. . .	. . .	0.081 ± 0.013	0.688 ± 0.007	53.4
7	7.50 ± 0.60	1.93 ± 0.05	17.0 ± 0.5	. . .	0.056 ± 0.02	0.305 ± 0.108	0.157 ± 0.020	0.945 ± 0.010	67.2

Notes.
[a] In units of 10^{-16} W m^{-2}.
[b] This line was measured from SH ([S III]18.7 μm) and LH maps ([S III]33.5 μm and [Si II]34.8 μm). The SH maps have an area of 1164 arcsec^2 for the ring, 684 arcsec^2 for Enuc N, and 337 arcsec^2 for Enuc S. The LH maps have an area of 1392 arcsec^2 for the ring, 2188 arcsec^2 for Enuc N, and 1193 arcsec^2 for Enuc S.
[c] The FIR flux was calculated as FIR = TIR/2, with TIR calculated from Dale & Helou (2002) using *Spitzer* MIPS 24 μm and *Herschel* PACS 70 μm and 160 μm.

[O I]63 μm maps and the 70 μm and 100 μm PACS images convolved to the PACS 160 μm PSF using the convolution recipe described in Aniano et al. (2011). Due to low signal to noise (S/N), [O I]63 μm could only be measured in the ring and Enuc S. The total luminosity of [C II]158 μm and [O I]63 μm in the ring is $L_{\rm [C II]} \sim 1.4 \times 10^8\,L_\odot$ and $L_{\rm [O I]} \sim 5.4 \times 10^7\,L_\odot$, respectively. In Table 4 we present all the [C II], [O I], and PAH fluxes measured for all the regions, as well as ionic lines measured at hi-res, [S III]18 μm, [S III]33.5 μm, and [Si II]34.5 μm.

In Figure 7 (upper) we plot the ratio [C II]158 μm/ PAH(5.5–14 μm) as a function of 70 μm/100 μm flux ratios, based on PACS photometry for the ring and the two extranuclear maps at a resolution of 11″ beam^{-1}. The 70 μm/100 μm flux ratio is a commonly used indicator of dust temperature. Each data point is one of the 12″ square regions (∼1.1 kpc). There is a clear difference between the ring and the extranuclear positions in both [C II]158 μm/PAH(5.5–14 μm) and 70 μm/100 μm. We performed a Kolmogorov–Smirnov (K-S) test to determine the significance of this difference. The
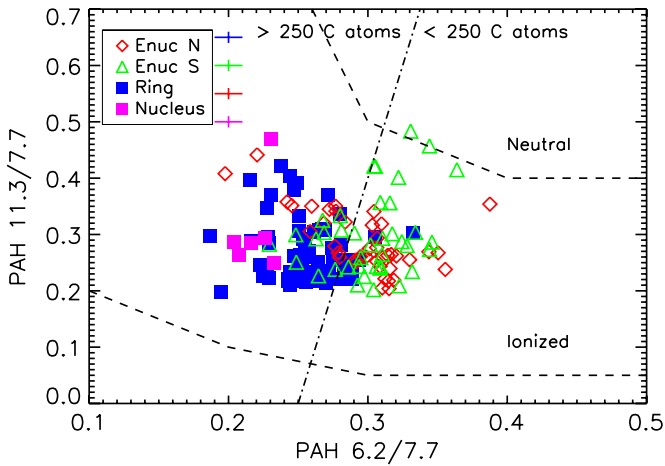
Figure 5. Plot of the $11.3\,\mu\text{m}/7.7\,\mu\text{m}$ PAH flux ratio as a function of $6.2\,\mu\text{m}/7.7\,\mu\text{m}$ PAH flux ratio. Each point corresponds to a $3\rlap.''7 \times 3\rlap.''7$ pixel region in the SL maps. The dashed lines indicate ionization states of the PAH molecules. Data from the ring are in blue, the nucleus are in violet, Enuc N are in red, and Enuc S are in green. The error bars indicate the average uncertainties for each region. The dash-dotted line indicates the position of the molecules formed by 250 carbon atoms. This figure is adapted from Draine & Li (2001).

(A color version of this figure is available in the online journal.)
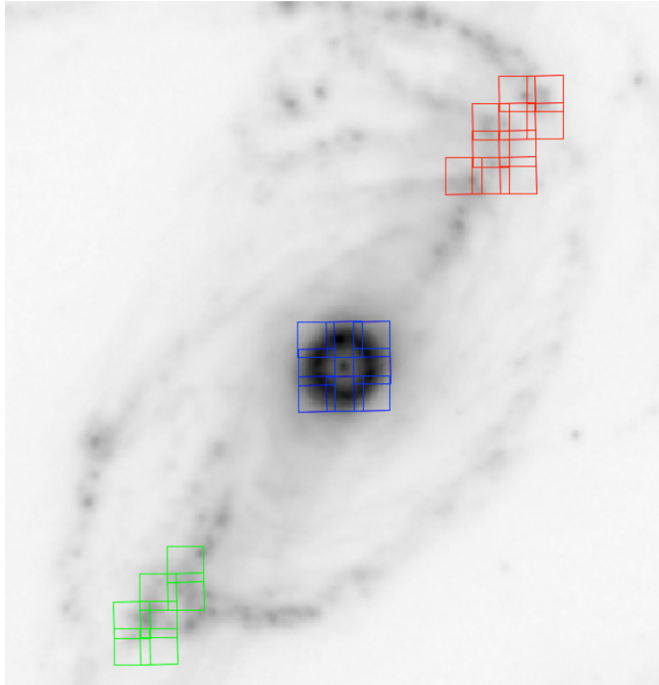
Figure 6. The $12'' \times 12''$ square apertures selected for measuring the [C II]158 μm, [O I]63 μm, PAH(5.5–14 μm), 70 μm, and 100 μm fluxes in the ring (blue), Enuc N (red), and Enuc S (green), overlaid on an IRAC 8 μm image of NGC 1097. North is up.

(A color version of this figure is available in the online journal.)

D-statistic is 0.85, with a probability of 0.029% of the ring and Enuc S belonging to the same population. The difference between the two regions is therefore significant. For the ring, the median [C II]158 μm/PAH(5.5–14 μm) is $\sim$0.034 and for the Enucs $\sim$0.053, about a factor of $\sim$1.6 above the median ring value. The 70 μm/100 μm ratio ranges between 0.35 and 0.55 for Enuc N and S, and between 0.70 and 0.80 for the ring.
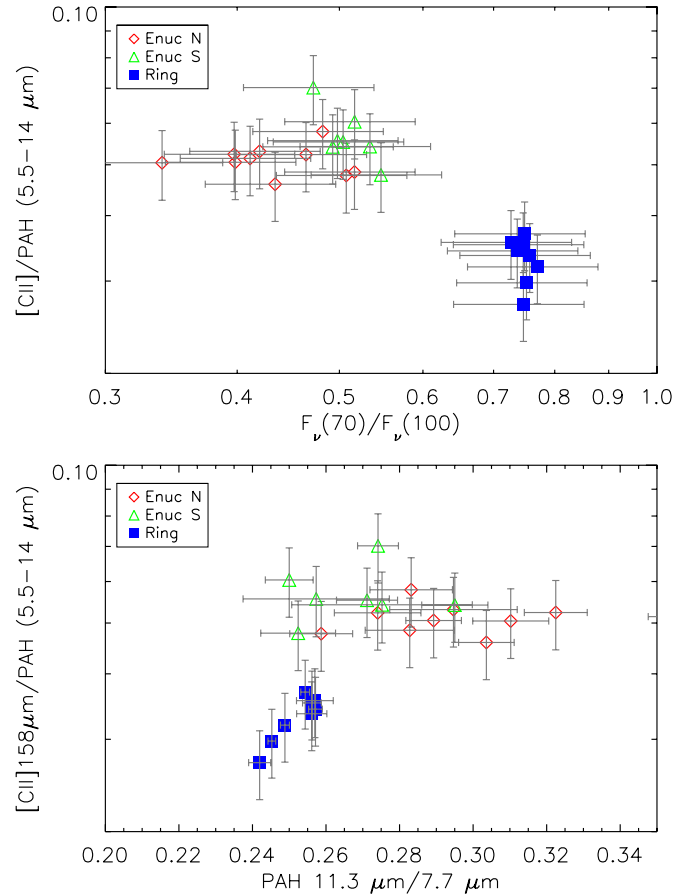
Figure 7. Top: plot of the ratio [C II]158 μm/PAH(5.5–14 μm) as a function of the 70 μm/100 μm flux ratio. Bottom: plot of the ratio [C II]158 μm/PAH(5.5–14 μm) as a function of the 11.3/7.7 PAH ratio. Each point was calculated for a resolution of $11''$ beam^{-1}.

(A color version of this figure is available in the online journal.)

The dust is warmer and the [C II]158 μm/PAH(5.5–14 μm) is lower in the ring than in the Enucs. If we consider the total infrared emission between 5 and 10 μm, $F(5.5–10\,\mu\text{m})$, we can compare our results with Helou et al. (2001), in which [C II]158 μm/$F(5.5–10\,\mu\text{m})$ is constant, suggesting that photoelectrons liberated from PAH grains were responsible for heating the gas. Our values for [C II]/$F(5–10\,\mu\text{m})$ are $\sim$50% lower in the ring than in the Enucs. In Figure 7 (lower) we plot the same ratio [C II]158 μm/PAH(5.5–14 μm) now as a function of the 11.3/7.7 μm PAH ratio, at a common resolution of $11''$ beam^{-1}. The distribution of 11.3/7.7 μm PAH ratios in the ring is narrower than in the Enuc regions, and has a median value of 0.25, lower than the median value of 11.3/7.7 μm in the Enuc regions, which is 0.28. This could be due to the fact that the PAH emission in the ring is more ionized. We performed a Spearman rank correlation test, and the result is 0.33, revealing a weak correlation between [C II]158 μm/PAH(5.5–14 μm) flux ratio and the 11.3/7.7 μm PAH ratio. However, this apparent correlation is only due to the lower [C II]158 μm/PAH(5.5–14 μm) values in the ring, whereas the Enuc values of [C II]158 μm/PAH(5.5–14 μm) appear to be insensitive to the local 11.3/7.7 μm flux ratio. Therefore, it is not clear that the difference in [C II]158 μm/PAH(5.5–14 μm) between the ring and the Enucs is due to a variation of the PAH ionization. Note that the 11.3/7.7 μm data points shown in Figure 7 were measured over a much wider area, and therefore are an average of the data
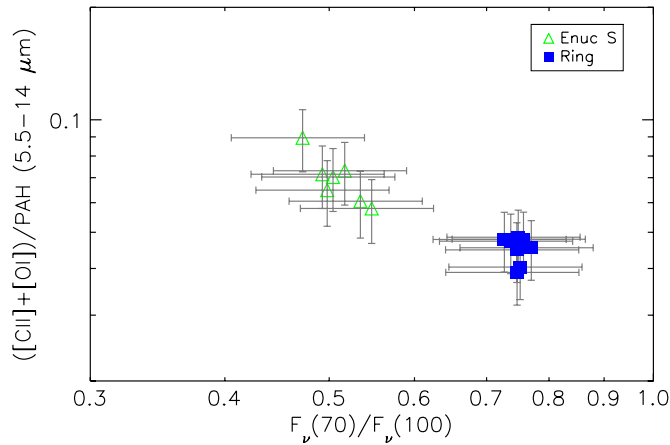
Figure 8. Plot of the ratio ([C II]158 μm+[O I]63 μm)/PAH(5.5–14 μm) as a function of the 70 μm/100 μm flux ratio. Each point was calculated for a resolution of 11″ beam^{-1}.

(A color version of this figure is available in the online journal.)

points in Figures 4 and 5. This accounts for the narrower range of 11.3/7.7 μm values in Figure 7. [O I]63 μm can also be an important coolant in warmer regions. In Figure 8 we plot the sum of the [C II]158 μm and [O I]63 μm emission over the PAH flux between 5 and 14 μm against the 70 μm/100 μm flux ratio. We measured the [O I]63 μm fluxes after smoothing the [O I]63 μm image to the 160 μm PACS PSF (a resolution of approximately 11″), using kernels from Aniano et al. (2011). Here we exclude Enuc N due to low S/N in the [O I]63 μm line. The gap between the Enuc S and the ring in ([C II]158 μm+[O I]63 μm)/PAH is smaller than in [C II]158 μm/PAH, with a median of ∼0.047 for the ring and ∼0.070 for Enuc S. [O I]63 μm therefore has a much larger role in the cooling of the gas in the ring than in Enuc S. This is consistent with the behavior of ([C II]158 μm+ [O I]63 μm)/PAH in the galaxies as reported by Helou et al. (2001). Both the ring and the Enucs in NGC 1097 are within the range of parameters studied in Helou et al. (2001). They calculate [C II]/F(5–10 μm) for a sample of star-forming galaxies using global averages and shows no trend with 60 μm/100 μm. However, they find a large scatter in ([C II]+[O I])/F(5–10 μm) as a function of 60 μm/100 μm. What we are uncovering is the inherent variations within galaxies that might drive the scatter in this relation. We should note that all the measurements are affected by the uncertainty on the PACS beam size and the shape of the PSFs, quantified in Aniano et al. (2011).

Another important cooling line is [Si II] at 34.8 μm. With a critical density ∼10^5 cm^{-3} for collisions with neutral hydrogen and ∼10^2 cm^{-3} for collisions with electrons, and a low ionization potential of 8.15 eV, this line comes from a wide variety of regions, such as ionized gas and warm atomic gas, PDRs, and X-ray-dominated regions (XDRs; Hollenbach & Tielens 1999). H II regions represent a large fraction of [Si II]34.8 μm emission in the ring (between 30% and 60%; e.g., Nagao et al. 2011). We used an [Si II]34.8 μm image of the ring and Enuc S, and convolved it to the 160 μm *Herschel*-PACS beam using theoretical *Spitzer*-IRS PSFs made with STinyTim and *Herschel* PSFs calculated by Aniano et al. (2011). From these images we measured a luminosity $L_{[Si II]} \sim 4 \times 10^8\,L_\odot$ in the ring and $L_{[Si II]} \sim 4 \times 10^7\,L_\odot$ in Enuc S, so $L_{[Si II]} \sim 1.6 \times L_{[O I]}$. This extra cooling would raise the ring and Enuc S in Figure 8.

In Figure 9 we show a plot of [C II]158 μm/FIR as a function of the 70 μm/100 μm flux ratio, with the data points
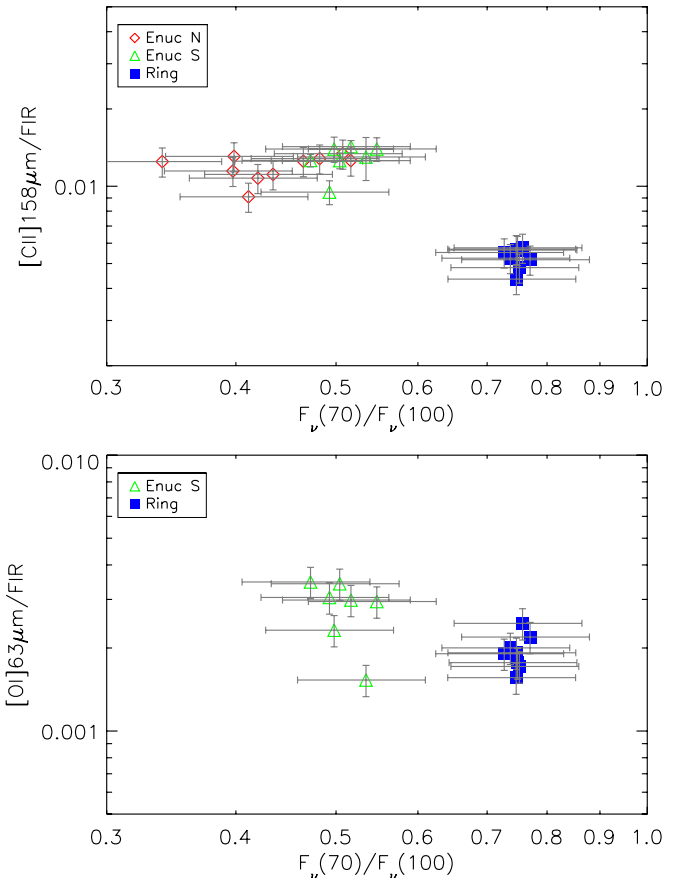
Figure 9. Top: plot of [C II]158 μm/FIR as a function of the 70 μm/100 μm flux ratio. Bottom: plot of [O I]63 μm/FIR as a function of the 70 μm/100 μm flux ratio.

(A color version of this figure is available in the online journal.)

calculated at a common beam size (11″). FIR is the far-infrared luminosity, estimated as FIR = TIR/2, with TIR as the total infrared luminosity, which was calculated using the formula by Dale & Helou (2002), replacing the 70 μm and 160 μm flux by PACS 70 μm and 160 μm fluxes. The ring has a [C II]158 μm/FIR which is a factor of ∼3 lower than the Enuc regions, and this difference is much larger than the factor of ∼1.5 in [C II]158 μm/PAH(5.5–14 μm) between the ring and the Enucs. This effect has been associated with regions with high G_0/n where other cooling lines are enhanced, such as [O I]63 μm (Malhotra et al. 2001). The [C II]158 μm/FIR in the ring is similar to the value in other star-forming galaxies observed by *ISO* such as NGC 1482, which has [C II]158 μm/FIR ∼ 0.004 and NGC 1569, with [C II]158 μm/FIR ∼ 0.0027 (Malhotra et al. 2001). In Figure 9 (bottom) we plot [O I]63 μm/FIR for the ring and Enuc S. We see that [O I]63 μm/FIR is still lower for the ring, but [O I]63 μm contributes at most ∼25% of the [C II]158 μm+[O I]63 μm flux in the Enucs and ∼30% of the [C II]158 μm+[O I]63 μm flux in the ring. Although some of the cooling indeed goes through [O I]63 μm, it cannot fully compensate for the difference between the ring and the Enuc S in [C II]158 μm/FIR. The decrease in [C II]158 μm/FIR can be caused not only by cooling via other emission lines, but also by absorption of ionizing photons by dust, low PAH abundance due to PAH destruction or coagulation into larger grains, collisional suppression of [C II]158 μm, or the [C II]158 μm being optically thick.

9
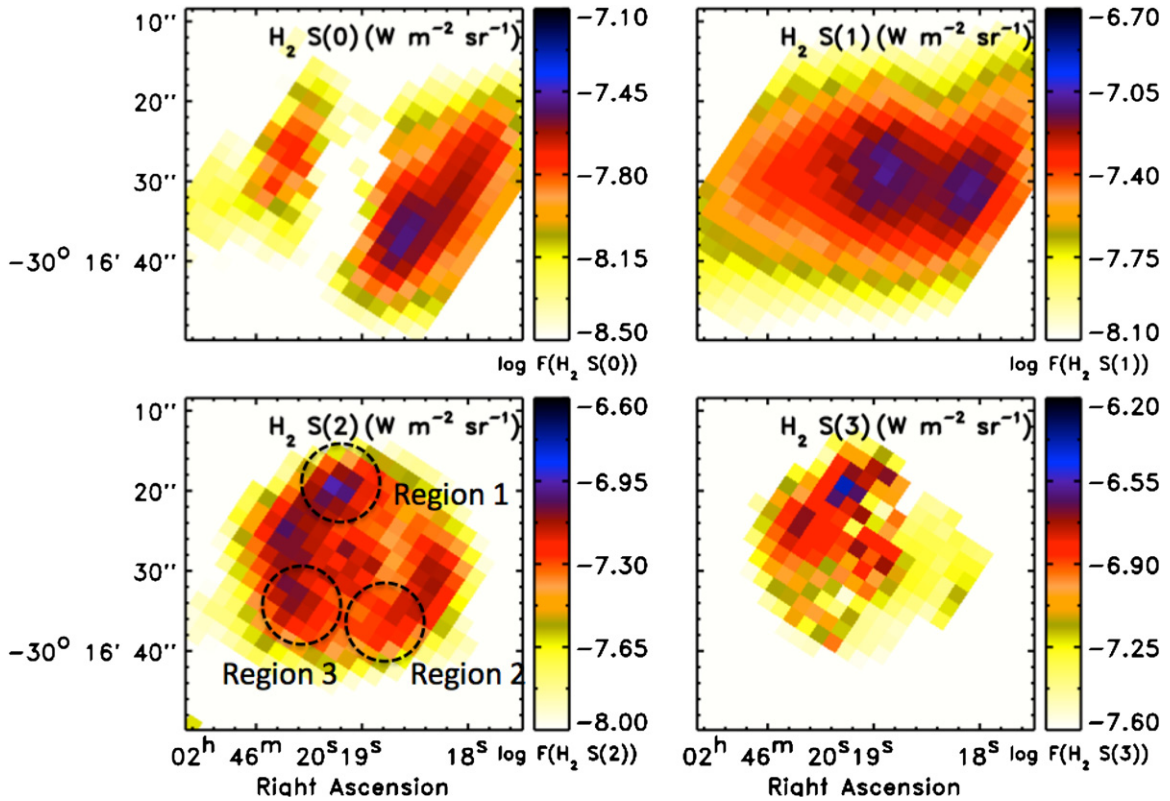
Figure 10. Maps of the H$_2$ S (0), H$_2$ S(1), H$_2$ S(2), and H$_2$ S(3) at 28.2 μm, 17.0 μm, 12.3 μm, and 9.7 μm, respectively. "Region 1," "Region 2," and "Region 3" denote three regions selected along the ring (see descriptions in the text). All images are at their native resolutions, i.e., 6″.8, 4″.1, 3″.1, and 2″.4, respectively, if we approximate the IRS PSFs as Gaussians. North is up.

(A color version of this figure is available in the online journal.)

3.4. Warm H$_2$ Emission

Figure 10 shows flux maps of the H$_2$ rotational lines from $S(0)$ to $S(3)$ at their native resolution, extracted pixel by pixel with PAHFIT. Most of the $S(0)$ flux is emitted from two spots in the ring that coincide with the intersection of the bar with the ring. The $S(1)$ line flux is also emitted from these spots, but also peaks at the nucleus. In $S(2)$ and $S(3)$, the flux peaks at a region in the NE part of the ring, where the main Hα and FIR lines are emitted (Beirão et al. 2010), but there is also some emission from the nucleus.

With the H$_2$ emission maps, we can estimate the gas temperature, column density, and mass distributions by fitting the H$_2$ fluxes using the Boltzmann equation (Rigopoulou et al. 2002), assuming that the ortho/para ratio is in local thermodynamical equilibrium. In Figure 11 we plot the excitation diagrams for the ring and nucleus of NGC 1097 (upper), and three selected ($\sim 10''$) regions on the ring (lower), with fits to the warm and hot H$_2$ phases. In this fit, 100 K was set as the lower temperature limit, as this is approximately the lowest temperature in a collisionally excited H$_2$ gas. Before the fit we convolved the $S(3)$, $S(2)$, and $S(1)$ images to a Gaussian with FWHM = 7″, which is the resolution at 28 μm. In Table 5 we present the properties of the warm H$_2$ gas in the ring, nucleus, and three 10″ diameter regions in the ring indicated in Figure 10. The lower temperature component in the nucleus has $\sim 2\%$ of the total H$_2$ luminosity of the nucleus, and therefore almost all the H$_2$ lines can be fitted with a single temperature. The ring is fitted with two components, a cool component with a temperature of 119 ± 11 K and a hot component with 467 ± 79 K. In the ring, the cool component emits 20% of the H$_2$ flux, so there

is a large quantity of gas in the ring at ~ 100 K that is not present in the nucleus. The lower plot in Figure 11 shows that the hot component varies between $T \sim 375$ and 470 K. Of the three selected regions, Region 2 has the highest fraction of emission from the cool component, $\sim 16\%$, and the lowest temperature of the warm component, perhaps indicative of a reservoir of colder gas in this region.

4. DISCUSSION

4.1. Physical Conditions in the Gas

To explore the physical conditions of the gas in the ring and Enuc regions, we use Kaufman et al. (2006) PDR models to determine the intensity of the radiation field and the density of the neutral gas using the [O I]63 μm and [C II]158 μm fine-structure lines. Our measurements of [C II]158 μm include an ionized gas contribution, where the gas is emitted from diffuse ionized regions. Therefore, one needs to subtract the ionized contribution to [C II]158 μm. This contribution can be estimated from measurements of the [N II] 122 μm and [N II]205 μm lines, which arise in diffuse ionized gas and H II regions. The [N II]122 μm/[N II]205 μm values published by Beirão et al. (2010) were affected by an incorrect relative spectral response function estimation, which affects the calibration of the continuum at $\lambda > 200$ μm. To correct this effect we have to multiply the [N II]205 μm flux by a correction factor of 4.5, which results in an [N II]205 μm/122 μm ~ 0.25 in the ring.

Using the estimated [N II]205 μm/[N II]122 μm value for the ring, we first calculate the fraction of [N II]122 μm from diffuse ionized gas (n_e = 10 cm^{-3}). Rubin et al. (1994)

Table 5
H$_2$ Model Parameters

Regions	Area (arcsec^2)	T (K)	Ortho/Para	N[a] (H$_2$)	M[b] (H$_2$)	L[c] (H$_2$)
Nucleus	96.8	100	1.587	8.71 ± 3.76	9.14 ± 3.94	0.06
		412 ± 19	3.000	0.46 ± 0.08	0.48 ± 0.09	2.58
Ring total	680.1	119 ± 11	1.972	16.0 ± 5.0	151.0 ± 47.2	2.75
		467 ± 79	2.999	0.15 ± 0.08	1.44 ± 0.72	12.6
Region 1	96.8	100	1.587	14.1 ± 7.1	14.8 ± 7.48	0.09
		470 ± 27	3.000	0.29 ± 0.06	0.30 ± 0.06	2.73
Region 2	96.8	100	1.587	41.3 ± 10.8	43.4 ± 11.3	0.28
		375 ± 23	2.995	0.40 ± 0.11	0.42 ± 0.11	1.52
Region 3	96.8	100	1.587	18.0 ± 7.8	18.9 ± 8.2	0.12
		401 ± 22	2.998	0.41 ± 0.09	0.43 ± 0.10	2.05

Notes.
[a] In units of 10^{20} cm^{-2}.
[b] In units of $10^6 M_\odot$.
[c] In units of $10^6 L_\odot$.
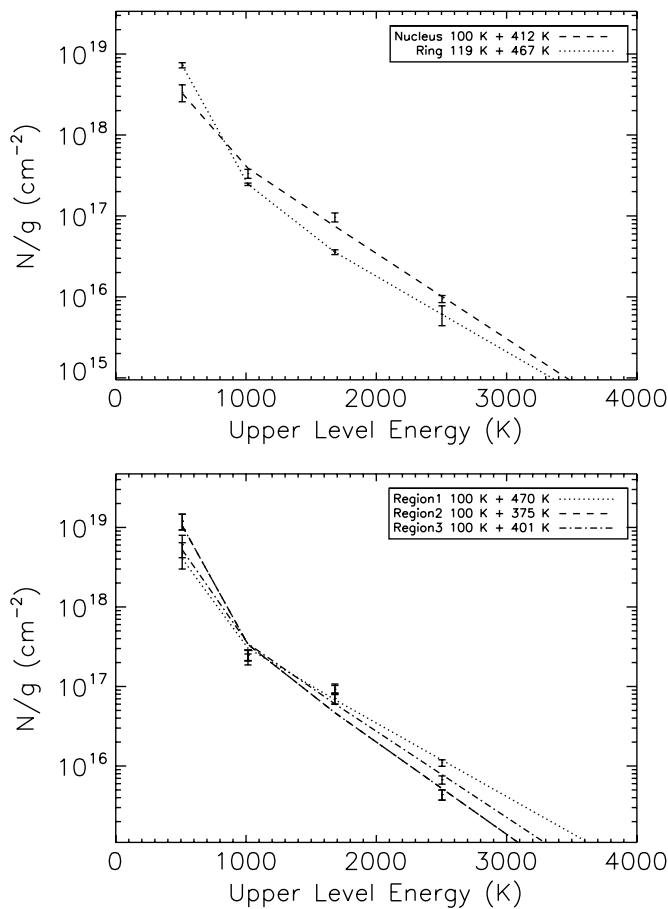
Figure 11. Top: mid-infrared H$_2$ excitation diagrams for the nucleus and the ring of NGC 1097. Bottom: excitation diagrams for the three regions selected along the ring and highlighted in Figure 10. The lines indicate the best fit to the H$_2$ data points (see Table 5).

calculate [N II]205 μm/[N II]122 μm ~ 1 for $n_e = 10$ cm^{-3} and [N II]205 μm/[N II]122 μm ~ 0.1 for $n_e = 10^3$ cm^{-3}. The average value of the [N II]205 μm/122 μm in the ring is ~ 0.25. Therefore, we estimate that the diffuse medium contributes $\sim 17\%$ of the observed [N II]122 μm emission in the ring. Using C$^+$ and N$^+$ abundances from Meyer et al. (1997) and Sofia et al. (2004), A values from Galavis et al. (1997, 1998) and collision strengths from Hudson & Bell (2005) and Blum &

Pradhan (1992), we derived a [C II]158 μm/[N II]122 μm ~ 4.8 in diffuse ionized gas and [C II]158/[N II]122 ~ 0.8 in the dense ionized gas. If 17% of the observed [N II]122 μm is emitted from the diffuse ionized gas, [C II]158 μm$_{ion}$ ~ 1.5[N II]122 μm. We can use this estimate to calculate the ionized gas contribution to [C II]158 μm. From Beirão et al. (2010), [C II]158 μm/[N II]122 ~ 4.5 in the ring, which suggests that $\sim 33\%$ of the [C II]158 μm flux in the ring is emitted from ionized gas and $\sim 67\%$ from PDRs. Note that this estimate is affected by the uncertainty on the [N II]205 μm/122 μm value, which is $\sim 50\%$.

Similarly, we can determine the maximum ionized gas fraction of the [C II]158 μm emission in Enuc S, and compare to the value for the ring estimated above. Because of low S/N, no measurement of [N II]205 μm was possible in Enuc N and S and no [N II]122 μm was possible in Enuc N. However, we can use [S III]18 μm/33 μm ratio as a tracer of density for regions with $n_e > 100$ cm^{-3}, and use the density estimated from this ratio to estimate the corresponding [N II]122 μm/[N II]205 μm (see Croxall et al. 2012). We measure [S III]18/33 ~ 1.2 in Enuc S. This corresponds to [N II]122 μm/[N II]205 μm ~ 8. Assuming 10 cm^{-3} for the diffuse component and 10^3 cm^{-3} for the dense component, we can estimate the diffuse gas contribution to [N II]122 μm/[N II]205 μm in Enuc S as $\sim 2.8\%$. Using these values, we get [C II]158 μm/[N II]122 ~ 0.9 for the ionized component in Enuc S, which is $\sim 5\%$ of the observed ratio, [C II]158 μm/[N II]122 ~ 17 (Beirão et al. 2010). Therefore, the ionized gas component accounts for $\sim 5\%$ of the [C II]158 μm flux in Enuc S. Enuc S therefore seems to have a much lower fraction of the observed [C II]158 μm emission coming from ionized regions than does the ring.

Using the neutral gas component of the [C II]158 μm flux and the [O I]63 μm flux for the ring and Enuc S, we estimate G_0 and n_H throughout these regions. We use the notation that G_0 is measured in units of the Habing radiation field (Habing 1968). We first assume that, after subtracting the ionized component, all the remaining [C II]158 μm emission and all [O I]63 μm and FIR flux are emitted from PDRs irradiated by massive stellar clusters. Following Kaufman et al. (2006), the grid in Figure 12 shows a variation of the incident radiation field G_0 between ~ 80 in the Enuc S region and 800 in the ring. The gas density is 10^3–$10^{3.5}$ cm^{-3} in both regions. These values are similar to local star-forming spiral galaxies such as NGC 695 and NGC 3620 (Malhotra et al. 2001). The density is a factor of 10 lower than that in M82, but the value of G_0 in the ring is
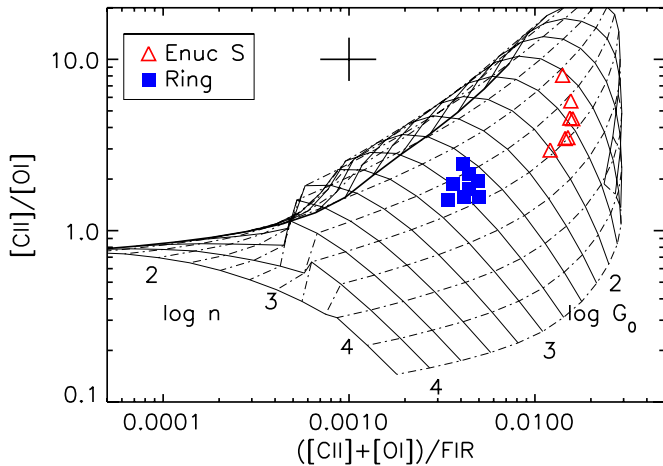
Figure 12. Plot of [C II]158 μm/[O I]63 μm as a function of ([C II]158 μm+[O I]63 μm)/FIR luminosity ratios, emitted from a PDR according to a grid of G_0 and n_H, for the ring and Enuc S, as defined in Section 3.3. For clouds illuminated on all sides by G_0, the observed ([O I]63 μm + [C II]158 μm)/FIR ratio is the ratio of the escaping intensities of line photons to grain continuum for each cloud. This corresponds to I([O I] 63 μm + [C II] 158 μm)/2 × I_{FIR}, where I_{FIR} = 2 × 1.3 × $10^{-4}G_0$ erg cm^{-2} s^{-1} sr^{-1}. Only [O I]63 μm data from Enuc S and the ring are available. The error bars represent the average uncertainties derived from photometric errors.

(A color version of this figure is available in the online journal.)

comparable to M82 (Kaufman et al. 1999). The larger G_0 in the ring presumably signals an increased ionization parameter, which measures the number of ionizing photons per hydrogen atom. This is consistent with our estimate above that ∼33% of the [C II]158 μm originates from ionized regions.

However, when considering detailed fits of the dust SED of the ring instead of just the FIR emission-line ratios, a different picture of the intensity of the ionizing field emerges. Using Draine & Li (2007) models, Aniano et al. (2011) estimate that only 25% of the TIR is being emitted from regions where $G_0 > 10^2$. For Enuc S this fraction is only about 8%. Therefore, if we use these estimates for the infrared emission together with the PDR models of Kaufman et al. (2006), we predict a lower ionizing radiation field intensity for the ring, much closer to a value of $G_0 \sim 10^{2.3}$, with a corresponding $n_H \sim 10^{3.5}$ cm^{-3}. These significantly different estimates for the G_0 and n_H in the ring PDRs have important implications for the production of the warm H$_2$ emission we measure in the IRS data, and we will carry both of these estimates forward when discussing the source of the H$_2$ emission in Section 4.3. For Enuc S, Aniano et al. (2011) predict a PDR fraction of the TIR flux of ∼8% in Enuc S. This will make $(F($[C II]$)+F($[O I]$))$/FIR > 0.1 in Enuc S, out of the range modeled by Kaufman et al. (2006) for PDR regions. All the line emission could be coming from the diffuse ISM and not PDRs in Enuc S, and therefore we cannot predict the G_0 and n_H.

Recently, using *Herschel*/PACS to observe a number of infrared starburst galaxies, Graciá-Carpio et al. (2011) established a correlation between [C II]158 μm/FIR and regions with high star formation efficiency, L_{FIR}/M_{H_2}, where [C II]158 μm/FIR drops only when $L_{FIR}/M_{H_2} > 80 L_\odot/M_\odot$. Based on PACS 70 μm and 100 μm fluxes from Sandstrom et al. (2010) and CO 2–1 fluxes from Hsieh et al. (2008; assuming $X_{CO} = 3.0 \times 10^{20}$ cm^{-2} (K km s^{-1})$^{-1}$ and $R_{21} \sim 1.3$), we calculate $L_{FIR}/M_{H_2} \sim 50 L_\odot/M_\odot$ in the ring of NGC 1097, lower than the value of L_{FIR}/M_{H_2} for which [C II]158 μm/FIR decreases for the luminous starbursts in Graciá-Carpio et al. (2011). Although [C II]158 μm/FIR is lower in the ring than Enucs, it is

consistent with other starburst galaxies having similar values of L_{FIR}/M_{H_2}.

4.2. Gas Heating Efficiency and PAH Abundance

Theoretical studies have shown that the extent of grain charging, and therefore the efficiency of photoelectric heating, is not only dependent on environmental conditions, but also on grain size and grain species. Bakes & Tielens (1994) estimated that approximately half of the heating is from grains with less than about 1500 C atoms (∼15 Å). Using *IRAS* and *ISO* observations of the [C II]158 μm, [O I]63 μm, and H$_2$ lines, Habart et al. (2004) quantified the photoelectric efficiencies attributed to the PAH, very small grains (VSGs), and big grains (BGs) populations in the ρ Oph cloud, finding $\epsilon_{PAH} = 3\%$, $\epsilon_{VSG} = 1\%$, and $\epsilon_{BG} = 0.1\%$, respectively. This suggests that PAHs are the most efficient gas heating channel in star-forming galaxies and therefore drive the heating of the neutral gas regions (Watson 1972; Hollenbach & Tielens 1999). Indeed, Helou et al. (2001) showed that the PAH contribution to the gas heating appears constant in galaxies with increasing $F(60 \mu m)/F(100 \mu m)$, and dominant over the contribution of large grains, based on the relatively constant [C II]158 μm/PAH against a rapidly falling [C II]158 μm/FIR. This suggests that PAHs dominate the heating of the [C II]-emitting gas (via the photoelectric effect), while large grains dominate the FIR emission from galaxies (Malhotra et al. 2001).

A decrease in the [C II]158 μm relative to the FIR emission could also be caused by a decrease in the photoelectric gas heating efficiency associated with highly charged grains. While the [C II]158 μm/PAH(5.5–14 μm) is lower in the ring than in the Enucs in NGC 1097, we find no correlation between [C II]158 μm/PAH(5.5–14 μm) and the 11.3/7.7 μm PAH ratio, which measures PAH ionization. Although the average 11.3/7.7 μm PAH ratio is lower on average in the ring than in the Enucs, the regions in the Enucs with similar 11.3/7.7 μm PAH ratios have clearly higher [C II]158 μm/PAH(5.5–14 μm). This means that the variation of [C II]158 μm/PAH(5.5–14 μm) between the Enucs and the ring cannot be attributed solely to PAH ionization. However, we have seen in Figure 8 that [O I]63 μm partially compensates for the decrease of [C II]158 μm/PAH(5.5–14 μm) ratio in the ring. As seen in Section 3.3, ([C II]158 μm+[O I]63 μm)/PAH in Enuc S is ∼1.5 times higher than in the ring. After subtracting the ionized gas contribution to the [C II]158 μm emission, the heating efficiency ([C II]158 μm+[O I]63 μm)/PAH in Enuc S is ∼1.9 times higher than in the ring. So by subtracting the ionized gas component, we obtain an estimate of the difference in the gas heating efficiency between the ring and Enuc S which is much larger than our previous estimates.

Since the [Si II]34.8 μm line is also a major coolant we can include this emission in the overall energy budget of NGC 1097. Following Kaufman et al. (2006), the [Si II]34.8 μm flux emitted from PDRs increases relative to the [Si II]34.8 μm flux emitted from H II regions as the electron density n_e increases. The [Si II]34.8 μm line can be as luminous as the [O I]63 μm, and ([C II]+[O I]+[Si II])/PAH(5.5–14 μm) is similar in the ring and in Enuc S. However, this ratio would not represent accurately the gas heating efficiency, as it includes also the contributions to [C II]158 μm and [Si II]34.8 μm from the ionized gas. Therefore, we can only estimate upper limits on the photoelectric heating efficiency of the PAHs in the PDRs using ([C II]$_{neut}$ + [O I] + [Si II])/PAH(5.5–14 μm) for the ring and Enuc S, respectively, with [C II]$_{neut}$ representing the neutral gas component of
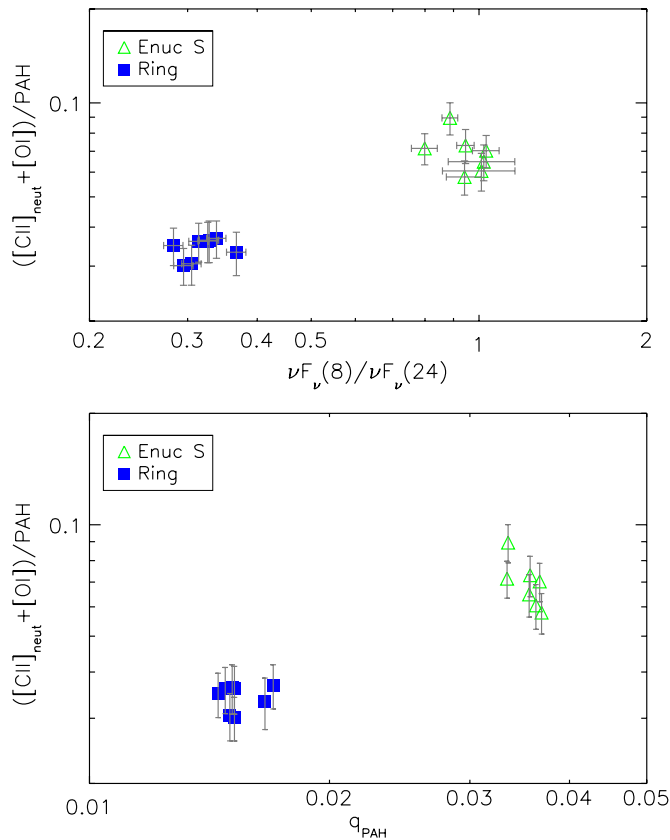
Figure 13. Upper: plot of the ([C II]158 μm+[O I]63 μm)/PAH(5.5–14 μm) ratio as a function of $F_\nu(8\,\mu$m)/$F_\nu(24\,\mu$m) as traced by *Spitzer*-IRAC bands for the regions defined in Section 3.3. Lower: plot of the ([C II]158 μm+[O I]63 μm)/PAH(5.5–14 μm) ratio as a function of the PAH mass abundance q_{PAH}, calculated using the dust emission models of Draine & Li (2007).

(A color version of this figure is available in the online journal.)

the [C II]158 μm emission, calculated in Section 4.1. This results in a PAH photoelectric heating efficiency of $5.2\% \pm 0.3\%$ in the ring and $7.7\% \pm 0.8\%$. Thus, we have seen that adding [Si II]34.8 μm brings down the difference in photoelectric heating efficiency between the ring and Enuc S to 3σ for ([C II]$_{\mathrm{neut}}$ + [O I] + [Si II])/PAH(5.5–14 μm).

Using IRAC 8 μm and MIPS 24 μm photometry of the Large Magellanic Cloud (LMC), Rubin et al. (2009) noted that the ratio between the [C II]158 μm and the total infrared flux TIR decreases with decreasing $F(8\,\mu$m)/$F(24\,\mu$m), which they use as a measure of PAH/VSG flux in regions with bright PAH emission. Variations of the $F_\nu(8\,\mu$m)/$F_\nu(24\,\mu$m) ratio arise mainly from the destruction of PAHs in H II regions and heating of VSGs to high temperatures in regions with intense radiation fields. If PAHs are destroyed, their emission in the infrared (at 8 μm) decreases relative to the infrared emission from other grains (at 24 μm). In regions with $G_0 > 100$, $F_\nu(24\,\mu$m)/F_{TIR} will increase with starlight intensity, and the emission at 24 μm will increase relative to 8 μm. To verify if this is the case for NGC 1097, in Figure 13 (upper) we present a plot of the ([C II]+[O I])/PAH(5.5–14 μm) ratio for the ring and the Enuc N and S as a function of the $F_\nu(8\,\mu$m)/$F_\nu(24\,\mu$m) ratio, calculated from the IRAC 8 μm and MIPS 24 μm maps convolved to the PACS 160 μm beam size (Aniano et al. 2011). The average $F_\nu(8\,\mu$m)/$F_\nu(24\,\mu$m) ratio in the ring in NGC 1097 is $\sim$0.37 $\pm$ 0.015, the same found for locations in the LMC

with the highest [C II]158 μm surface brightness, whereas the average values of $F_\nu(8\,\mu$m)/$F_\nu(24\,\mu$m) for Enuc N and S are $\sim$1.1 $\pm$ 0.1, which correspond to the average value observed in the LMC for similar [C II]158 μm surface brightness. The ring has both lower ([C II]158 μm+[O I]63 μm)/PAH and $F_\nu(8\,\mu$m)/ $F_\nu(24\,\mu$m) than the extranuclear regions. Therefore, the low ([C II]$_{\mathrm{neut}}$+[O I])/PAH(5.5–14 μm) and $F_\nu(8\,\mu$m)/$F_\nu(24\,\mu$m) might be due both to a lack of PAH grains and higher starlight intensity. We should note that $F_\nu(8\,\mu$m)/$F_\nu(24\,\mu$m) is not an independent parameter, as it is strongly correlated with $F_\nu(60\,\mu$m)/$F_\nu(100\,\mu$m).

Using Draine & Li (2007) models we can calculate the PAH mass fraction, defined as the fraction of grains with 1000 C atoms or less to all dust grains, as a result of calculating infrared emission spectra for dust heated by starlight. In Figure 13 (lower) we present a plot of the ([C II]$_{\mathrm{neut}}$+[O I])/ PAH(5.5–14 μm) ratio for the ring and the Enuc N and S as a function of the PAH mass fraction q_{PAH}, as measured in the q_{PAH} maps of NGC 1097 constructed by G. Aniano et al. (2012, in preparation). The trend for ([C II]$_{\mathrm{neut}}$+[O I])/PAH(5.5–14 μm) as a function of q_{PAH} is similar to the trend seen for the $F_\nu(8\,\mu$m)/$F_\nu(24\,\mu$m) ratio, with $q_{\mathrm{PAH}} \sim 0.018$ in the ring and $\sim$0.035 in the Enuc regions, a difference of a factor of two. The median q_{PAH} in the SINGS sample is also 0.035 (Draine et al. 2007). This suggests that the variation of the $F_\nu(8\,\mu$m)/ $F_\nu(24\,\mu$m) between the ring and the Enucs in NGC 1097 is a consequence of the variation of the PAH abundance relative to other types of grains. As long as PAHs dominate photoelectric heating and therefore [C II]158 μm and [O I]63 μm cooling, the ([C II]$_{\mathrm{neut}}$+[O I])/PAH(5.5–14 μm) ratio should not change with PAH abundance. As seen in Figure 13, ([C II]$_{\mathrm{neut}}$+[O I])/PAH(5.5–14 μm) decreases with decreasing q_{PAH} and $F_\nu(8\,\mu$m)/$F_\nu(24\,\mu$m) ratio. This could be a consequence of an increase of the role of VSGs on the photoelectric gas heating, as the PAH mass fraction decreases and the VSG abundance increases faster than the PAH abundance. A significant portion of [C II]158 μm and [O I]63 μm could be heated by VSGs, increasing ([C II]$_{\mathrm{neut}}$+[O I])/PAH(5.5–14 μm). On the other hand, it may be that when q_{PAH} increases, the PAH size distribution shifts to smaller sizes, which may have higher photoelectric heating efficiencies.

Figure 13 can also be interpreted by considering an alternative aspect of photoelectric heating efficiency. The efficiency of the photoelectric effect on a grain is traditionally defined (e.g., Hollenbach & Tielens 1999) as the ratio of gas heating to the grain UV absorption rate. Observationally, this is often approximated as the ratio of [C II]158 μm or [C II]158 μm+[O I]63 μm to the infrared emission from dust, assuming that [C II]158 μm and [O I]63 μm account for most of the cooling of the heated gas, and total infrared emission accounts for most of the UV absorbed by grains. However, photoelectric heating is dominated by the smallest grains in the ISM (Watson 1972; Jura 1976), whereas the total infrared emanates primarily from the larger grains. To avoid this complication, Helou et al. (2001) used [C II]158 μm/$F(5$–10 μm) as an estimate of efficiency limited to PAH, and showed that it varies considerably less than [C II]158 μm/FIR, thus demonstrating that the smallest grains, and more specifically PAHs, do indeed dominate photoelectric heating. However, these definitions do not account for the shifting balance of the diverse dust species in mass ratio or absorption of heating radiation. In Figure 13 we see a clear difference in q_{PAH}, the mass fraction of PAHs to large grains, between the starburst ring and Enuc S, much larger than the difference in

([C II]158 μm + [O I]63 μm)/PAH. A K-S test revealed that the difference in q_{PAH} between the ring and Enuc S is significant. Using dust mass and q_{PAH} maps from G. Aniano et al. (2012, in preparation), constructed using Draine et al. (2007) models, we are able to measure the total PAH mass in the ring and Enuc S and estimate the amount of [C II]158 μm and [O I]63 μm line emission per unit PAH mass in the ring and Enuc S. The values for ([C II]158 μm+[O I]63 μm)/M_{PAH} are 70 $L_\odot/M_\odot$ for Enuc S and 170 $L_\odot/M_\odot$ for the ring may be interpreted as rough estimates of the amount of photoelectric heating contributed per unit mass of PAHs. These values are for PDR gas only, i.e., the ionized gas fraction of [C II]158 μm was subtracted before deriving these quantities. These ratios suggest that per unit mass, PAHs in the ring are responsible for generating significantly more, by about a factor of two, [C II]158 μm and [O I]63 μm emission than PAHs in Enuc S, in spite of the slightly lower ([C II]158 μm+[O I]63 μm)/PAH flux ratio. In other words, the photoelectron production rate per unit mass of PAH is higher in the ring, even though the photoelectric heating efficiency is slightly lower. This difference in ratios is simply a reflection of the greater heating intensity available to the PAHs in the ring, making it possible for a PAH grain to process more photons per unit time, even if the photoelectric heating efficiency is lower, possibly because of increased ionization of the PAHs, or because of more frequent two-photon events. Since the PAHs are excited stochastically by one photon at a time, the increased production rate per unit mass can be seen as the result of approximately doubling the PAH excitation rate. This reflects how the mean starlight intensity $\langle U \rangle$ varies between the ring and Enuc S. Using $\langle U \rangle$ maps from G. Aniano et al. (2012, in preparation), constructed using Draine et al. (2007) models, we measured that $\langle U \rangle$ in the ring is ~3.6 times higher than in Enuc S, with an uncertainty of ~30%. Given the uncertainties involved, the ratio of $\langle U \rangle$ and the ratio of photoelectric production rate per unit mass between the ring and Enuc S are consistent.

4.3. What Is Exciting the H_2?

We have seen that the lower [C II]158 μm/PAH observed in the ring is partially compensated by the increase of the [O I]63 μm line, as it becomes a more efficient coolant in denser and warmer regions. However, another mechanism that may be responsible for gas heating in these regions is shock heating. Hollenbach & McKee (1989) predict fast (>30 km s^{-1}) J shocks to have strong [O I] emission. According to these models, the [O I]63 μm line is typically stronger than the [C II]158 μm line in regions where J-shock heating is important. However, [O I]63 μm/[C II]158 μm varies between 0.3 and 0.5 in the ring (Beirão et al. 2010). Therefore, fast shocks are not the dominant heating source of the ISM in the ring, at least not at scales probed by the PACS beam, although they could still be responsible for much of the [O I]63 μm emission. Slow (<30 km s^{-1}) C shocks could still be present in the ring, as they emit only weak [O I]63 μm (Hollenbach & McKee 1989).

By using the radiation field estimates from [C II]158 μm and [O I]63 μm, we can predict the H_2 emission from PDRs. Assuming the radiation field intensity G_0 calculated in Section 4.1, the H_2 fluxes from the ring can be reproduced using a pure PDR model by, e.g., Kaufman et al. (2006) with high-density molecular gas ($n \sim 10^5$ cm^{-3}). Such a molecular gas density is quite plausible, as Kohno et al. (2003) reported the existence of HCN (1–0) emission in the nucleus and ring, for which molecular gas densities of ~10^5 cm^{-3} are necessary (e.g., Meijerink et al. 2007). For $G_0 = 10^{2.25}$ and $n_H = 10^{3.5}$ calculated in
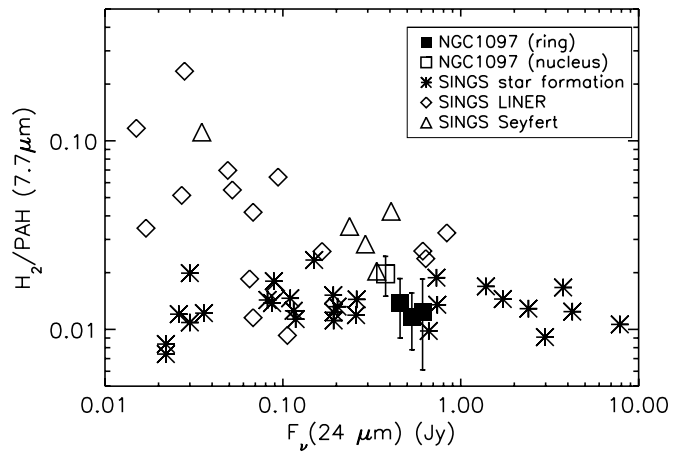
Figure 14. Ratio of H_2 luminosity summed over the $S(0)$–$S(3)$ lines to 7.7 μm PAH luminosity vs. $\nu F_\nu(24\,\mu$m) continuum luminosity. This ratio indicates the relative importance of mechanical heating and star formation power. The open square is the average for the nucleus, and the full squares are the values for three regions in the ring shown in Figure 10. All other points are ratios calculated for galaxies in the SINGS sample (Roussel et al. 2007).

Section 4.1, and assuming that the fraction of TIR flux from PDRs with these conditions is responsible for 25% of the total TIR emission, we predict that such PDRs will emit a total of H_2 flux of $F(H_2\ S(0)$–$S(3)) \sim 2.1 \times 10^{-16}$ W m^{-2}. Our measured total H_2 flux is $F_{H_2} \sim 1.3 \times 10^{-15}$ W m^{-2}, about a factor of six above the modeled value. Therefore, if most of the dust emission is coming from low $\langle U \rangle$ diffuse ISM, it is very difficult to account for the observed H_2 from the ring with intense PDRs. The H_2 lines must predominately come from some other type of region.

In the Milky Way there is increasing evidence that the diffuse ISM has pockets of warm H_2 that radiate in the H_2 rotational lines, where the excited H_2 is in excess of what would be produced by UV-pumping. Both H_2 and PAH emission have been observed in gas clouds illuminated by starlight (e.g., Habart et al. 2004). Ingalls et al. (2011) used Spitzer-IRS to show that high-latitude translucent clouds, illuminated by just the local starlight background ($\langle U \rangle \sim 1$), may contain small amounts of hot, collisionally excited H_2. In these clouds, $F(H_2\ S(2))/F(PAH7.7) \sim 0.002$ on average. In the ring of NGC 1097, $F(H_2\ S(2))/F(PAH7.7) \sim 0.0015$, so translucent clouds with low incident radiation are a plausible origin for the observed H_2 emission in the ring. The warm regions that produce the H_2 emission observed by Ingalls et al. (2011) will also radiate in [C II]158 μm and [O I]63 μm. Combining the H_2 measurements in Ingalls et al. (2011) with the [C II]158 μm results of Ingalls et al. (2002) gives $F(H_2\ S(0)$–$S(2))/[$C II$] \sim$ 0.4–1 for Milky Way translucent cloud positions detected in H_2 emission, which is much higher than the observed $F(H_2\ S(0)$–$S(2))/[$C II$] \sim 0.090$ in the ring. J. G. Ingalls & B. T. Draine (2012, in preparation) predict that the translucent clouds should have [O I]$/F(H_2\ S(0)$–$S(2)) < 0.19$, well below the observed [O I]$/F(H_2\ S(0)$–$S(2)) \sim 4.5$ in the ring. Thus, it seems possible that much of the H_2 rotational line emission from the ring could come from warm regions in the H_2 clouds, but these regions do not dominate the [C II]158 μm or [O I]63 μm emission we observe.

In Figure 14 we plot the ratio of H_2 luminosity in the 0–0 $S(0)$–$S(3)$ lines over $L_{PAH7.7}$ versus F_{24} for Regions 1, 2, and 3 in the ring and in the nucleus and compare these measurements with data from the SINGS sample of nearby galaxies (Roussel

et al. 2007). While the values for the ring are similar to those of star-forming galaxies (Roussel et al. 2007), which have a median ratio of $F(H_2) S(0)–S(3)/L(PAH7.7) = 0.011$, the nucleus is slightly larger, with a value of ~ 0.02, more consistent with the LINER and Seyfert nuclei in Roussel et al. (2007), although there is a large scatter among the galaxies with AGNs.

The nucleus of NGC 1097 has a weak AGN, apparently fed by an inflow of gas inside the ring (Prieto et al. 2005). It is possible, therefore, that X-rays from the AGN might contribute to the heating of the H_2 gas in the immediate vicinity of the nucleus. The cooling by H_2 rotational lines in XDRs is 2% of the total gas cooling (Maloney et al. 1996) for a temperature of 200 K, typical of warm H_2 that emits in the mid-infrared. At this temperature, the ratio of the first four rotational lines to the total rotational line luminosity is $L(H_2 S(0)–S(3))/L(H_2) = 0.58$. Combining the above factors, we estimate a maximum H_2 to X-ray luminosity ratio of $L(H_2 S(0)–S(3))/L_X(2–10 \,keV) = 0.01$. This ratio is conservative, since it assumes that all of the X-ray flux from the AGN is absorbed by the XDR. The nucleus of NGC 1097 has an X-ray luminosity of $L_X(2–10 \,keV) = 1.73 \times 10^{-15} \,W\,m^{-2}$ (Lutz et al. 2004). Therefore, the maximum H_2 luminosity should be $L(H_2) \sim 1.7 \times 10^{-17} \,W\,m^{-2}$, significantly lower than the measured $L(H_2 S(0)–S(3))$ in the nucleus, which is $\sim 2.3 \times 10^{-16} \,W\,m^{-2}$. Considering $L(H_2 S(0)–S(3))/L(H_2) = 0.58$, the contribution of X-rays for heating the H_2 is less than 5%. This is consistent with the near-infrared rotational–vibrational spectra taken across the nucleus by Reunanen et al. (2002).

Another possible source for H_2 heating are cosmic rays from supernovae. The energy released by the dissociation of each H_2 molecule by cosmic rays is $\sim 12 \,eV$, including the contribution from H_3^+ recombination and H_2 re-formation (e.g., Le Petit et al. 2006). To balance line cooling, the ionization rate per H_2, ζ_{H2}, must be few $\times \, 10^{-14} \,s^{-1}$. For such a rate, cosmic rays are the main destruction path of H_2 molecules. From Table 5 the total H_2 emission-line luminosity is $5.91 \times 10^{40} \,erg\,s^{-1}$ for the ring and $1.02 \times 10^{40} \,erg\,s^{-1}$ for the nucleus. Dividing this luminosity by the warm H_2 masses of $1.52 \times 10^8 \, M_\odot$ and $9.6 \times 10^6 \, M_\odot$, respectively, we can estimate a cooling rate through the H_2 lines of $3.2 \times 10^{-25} \,erg\,s^{-1}\,H_2^{-1}$ and $8.8 \times 10^{-25} \,erg\,s^{-1}\,H_2^{-1}$, respectively. The mass fraction of the gas in the molecular state depends on the rate of ionization and gas density ζ_{H2}/n_{H2}. Dividing the $H_2 S(0)–S(3)$ luminosity by the energy released per ionization, we estimate the required ionization rate, $\zeta_{H_2} \sim 1 \times 10^{-13} \,s^{-1}$ for the ring and $\zeta_{H_2} \sim 6 \times 10^{-13} \,s^{-1}$ for the nucleus. This value is larger than what is inferred from H_3^+ observations in the Milky Way, by a factor 200–1000 for the diffuse ISM (Indriolo et al. 2007) and by more than a factor 20 for the molecular gas within 200 pc from the Galactic center (Goto et al. 2008). It is therefore unlikely that the warm molecular gas in the ring and nucleus of NGC 1097 is heated solely by cosmic rays.

5. SUMMARY

In this paper we have attempted to understand the energetics and the physical conditions in the ISM in NGC 1097, using *Herschel*-PACS and *Spitzer*-IRS. Our goal was to study how heating and cooling of the ISM vary with the ISM phases, studying the origin of the variations of heating efficiency with dust temperature, and the properties of the warm H_2 in regions with different ISM heating mechanisms. We focused on the central region, where a ring of star formation and an AGN are located, and in two extranuclear regions at the ends of the bar, which we named Enuc N and S. We divided the ring, Enuc N, and Enuc S

regions into $12'' \times 12''$ regions. After subtracting the fraction of [C II]158 μm flux emitted from ionized gas, estimated as $\sim 33\%$ in the ring and $\sim 5\%$ in Enuc S, we examined the correlations between the [C II]158 μm/PAH ratio and the 70 μm/100 μm, the PAH ratio 11.3/7.7 μm. We implemented PDR models by Kaufman et al. (2006), and used the [C II]158 μm/[O I]63 μm ratio and ([C II]158 μm+[O I]63 μm)/FIR to plot a grid of the local FUV flux G_0, and the PDR density n, and diagnose the properties of the ISM on the ring and Enuc S. We also calculated the total H_2 and the PAH 7.7 μm fluxes in three regions in the ring and one centered in the nucleus to determine the origin of the warm H_2 excitation. As a result of our analysis we find the following.

1. Assuming that PDRs account for all [O I]63 μm, FIR flux and 67% of the [C II]158 μm, the average intensity of the radiation field G_0 is ~ 80 in Enuc S and ~ 800 in the ring. The gas density is 10^3–$10^{3.5}$ cm^{-3} in both regions. If instead 75% of the FIR flux in the ring arises from low starlight intensity regions and only 25% of the FIR flux arises from PDRs, then G_0 is $\sim 10^{2.3}$ and $n_H \sim 10^{3.5}$ in the ring.

2. The ratio [C II]158 μm/PAH(5.5–14 μm) is a factor of ~ 1.7 lower in the ring than in the Enuc regions and [C II]158 μm/FIR is a factor of ~ 4 lower in the ring than at the southern edge of the bar. The average 11.3/7.7 μm PAH ratio is lower in the ring than at the ends of the bar, suggesting a larger fraction of ionized grains in the starburst ring. However, no clear correlation was seen between the 11.3/7.7 μm PAH ratio and the [C II]158 μm/PAH(5.5–14 μm) ratio across the complete data set, implying that grain ionization is not the sole driver of the grain heating efficiency variations. The ratio ([C II]158 μm+[O I]63 μm)/PAH is still lower in the ring than the ends of the bar, although the difference is much smaller and the scatter larger than in [C II]158 μm/PAH(5.5–14 μm). After the removal of the ionized gas component of the [C II]158 μm emission and adding [Si II]34.5 μm, we calculated a gas heating efficiency in the ring of $\sim 5.2\%$ and $\sim 7.7\%$ in Enuc S. The amount of [C II]158 μm and [O I]63 μm line emission per unit PAH mass is roughly a factor of two larger in the ring than in Enuc S. Since the PAHs are excited stochastically by photons, the increased production rate per unit mass can be seen as the result of approximately doubling the PAH excitation event rate.

3. Using the [C II]158 μm and [O I]63 μm emission lines and total FIR emission from the ring used in conjunction with standard PDR models, the derived radiation field can account for nearly all the warm H_2 emission measured with *Spitzer*/IRS. However, if we incorporate the results of the dust SED modeling, which suggests nearly 75% of the FIR flux comes from dust heated by low starlight intensities in the diffuse ISM, there is a large excess of H_2 which cannot be excited in PDRs. In analogy to what is seen in the ISM of the Milky Way (Ingalls et al. 2011), we suggest this H_2 emission in the NGC 1097 ring may be coming from pockets of warm H_2 gas inside translucent molecular clouds in the diffuse ISM.

4. The $H_2 S(0)–S(3)$/PAH7.7 μm ratio is enhanced in the nucleus (the site of a weak AGN) relative to the ring by a factor of two, as is the fraction of warm ($T \sim 400 \,K$) molecular gas. X-rays and cosmic rays cannot provide more than 1%–5% of the energy necessary to produce the H_2 emission in the nucleus. Shock waves, possibly

associated with the central AGN, may be an important contributor to gas heating in the nucleus.

This paper is an example of the study that can be carried out by carefully combining *Herschel*/PACS and *Spitzer*/IRS data focusing on starburst rings or other resolved regions of enhanced star formation in nearby galaxies. In future papers we will explore the energy balance in the ISM of local star-forming galaxies within the KINGFISH sample and apply these methods of linking the atomic and molecular gas feature emission with the dust properties to more luminous starburst galaxies observed with *Spitzer* and *Herschel*.

REFERENCES

Allamandola, L. J., Hudgins, D. M., Bauschlicher, C. W., Jr., & Langhoff, S. R. 1999, A&A, 352, 659

Allamandola, L. J., Tielens, A. G. G. M., & Barker, J. R. 1985, ApJ, 290, 25

Aniano, G., Draine, B. T., Gordon, K. D., & Sandstrom, K. 2011, PASP, 123, 1218

Athanassoula, E. 1992, MNRAS, 259, 345

Bakes, E. L. O., & Tielens, A. G. G. M. 1994, in ASP Conf. Ser. 58, The First Symposium on the Infrared Cirrus and Diffuse Interstellar Clouds, ed. R. M. Cutri & W. B. Latter (San Francisco, CA: ASP), 412

Beirão, P., Armus, L., Appleton, P. N., et al. 2010, A&A, 518, 60

Blum, R. D., & Pradhan, A. K. 1992, ApJS, 80, 425

Brandl, B. R., Bernard-Salas, J., Spoon, H. W. W., et al. 2006, ApJ, 653, 1129

Contursi, A., Kaufman, M. J., Helou, G., et al. 2002, AJ, 124, 751

Croxall, K., Smith, J. D., Wolfire, M. G., et al. 2012, ApJ, 747, 81

Dale, D. A., Bendo, G. J., Engelbracht, C. W., et al. 2005, ApJ, 633, 857

Dale, D. A., & Helou, G. 2002, ApJ, 576, 159

Dale, D. A., Smith, J. D. T., Schlawin, E. A., et al. 2009, ApJ, 693, 1821

Davies, R. I., Maciejewski, W., Hicks, E. K. S., et al. 2009, ApJ, 702, 114

Draine, B. T., Dale, D. A., Bendo, G., et al. 2007, ApJ, 663, 866

Draine, B. T., & Li, A. 2001, ApJ, 551, 807

Draine, B. T., & Li, A. 2007, ApJ, 657, 810

Fathi, K., Storchi-Bergmann, T., Riffel, R., et al. 2006, ApJ, 641, L25

Galavis, M. E., Mendoza, C., & Zeippen, C. J. 1997, A&AS, 123, 159

Galavis, M. E., Mendoza, C., & Zeippen, C. J. 1998, A&AS, 133, 245

Gerin, M., Nakai, N., & Combes, F. 1988, A&A, 203, 44

Goto, M., Usuda, T., Nagata, T., et al. 2008, ApJ, 688, 306

Graciá-Carpio, J., Sturm, E., Hailey-Dunsheath, S., et al. 2011, ApJ, 728, 7

Habart, E., Boulanger, F., Verstraete, L., Walmsley, C. M., & Pineau des Forêts, G. 2004, A&A, 414, 531

Habing, H. J. 1968, Bull. Astron. Inst. Neth., 19, 421

Helou, G., Malhotra, S., Hollenbach, D. J., Dale, D. A., & Contursi, A. 2001, ApJ, 548, 73

Helou, G., Roussel, H., Appleton, P., et al. 2004, ApJS, 154, 253

Hollenbach, D. J., & McKee, C. F. 1989, ApJ, 342, 306

Hollenbach, D. J., & Tielens, A. G. G. M. 1999, Rev. Mod. Phys., 71, 173

Hony, S., Van Kerckhoven, C., Peeters, E., et al. 2001, A&A, 370, 1030

Hsieh, P.-Y., Matsushita, S., Lim, J., Kohno, K., & Sawada-Satoh, S. 2008, ApJ, 683, 70

Hudson, C. E., & Bell, K. L. 2005, A&A, 430, 225

Indriolo, N., Geballe, T. R., Oka, T., & McCall, B. J. 2007, ApJ, 671, 173

Ingalls, J. G., Bania, T. M., Boulanger, F., et al. 2011, ApJ, 743, 174

Ingalls, J. G., Reach, W. T., & Bania, T. M. 2002, ApJ, 579, 289

Jura, M. 1976, ApJ, 204, 12

Kaufman, M. J., Wolfire, M. G., & Hollenbach, D. J. 2006, ApJ, 644, 283

Kaufman, M. J., Wolfire, M. G., Hollenbach, D. J., & Luhman, M. L. 1999, ApJ, 527, 795

Kennicutt, R. C., Bendo, G., Engelbracht, C., et al. 2003, PASP, 115, 928

Kohno, K., Ishizuki, S., Matsushita, S., Vila-Vilaró, B., & Kawabe, R. 2003, PASJ, 55, 1

Kotilainen, J. K., Reunanen, J., Laine, S., & Ryder, S. D. 2000, A&A, 353, 834

Leger, A., & Puget, J. L. 1984, A&A, 137, L5

Le Petit, F., Nehmé, C., Le Bourlot, J., & Roueff, E. 2006, ApJS, 164, 506

Lutz, D., Maiolino, R., Spoon, H. W. W., & Moorwood, A. F. M. 2004, A&A, 418, 465

Malhotra, S., Helou, G., Stacey, G., et al. 1997, ApJ, 491, L27

Malhotra, S., Kaufman, M. J., Hollenbach, D., et al. 2001, ApJ, 561, 766

Maloney, P. R., Hollenbach, D. J., & Tielens, A. G. G. M. 1996, ApJ, 466, 561

Mason, R. E., Levenson, N. A., Packam, C., et al. 2007, ApJ, 659, 241

Meijerink, R., Spaans, M., & Israel, F. 2007, A&A, 461, 793

Meyer, D. M., Cardelli, J. A., & Sofia, U. J. 1997, ApJ, 490, 103

Nagao, T., Maiolino, R., Marconi, A., & Matsuhara, H. 2011, A&A, 526, A149

Poglitsch, A., Waelkens, C., Geis, N., et al. 2010, A&A, 518, L2

Prieto, M. A., Maciejewski, W., & Reunanen, J. 2005, AJ, 130, 1472

Reunanen, J., Kotilainen, J. K., & Prieto, M. A. 2002, MNRAS, 331, 154

Rigopoulou, D., Kunze, D., Lutz, D., Genzel, R., & Moorwood, A. F. M. 2002, A&A, 389, 374

Roussel, H., Helou, G., Hollenbach, D. J., et al. 2007, ApJ, 669, 959

Rubin, D., Hony, S., Madden, S. C., et al. 2009, A&A, 494, 647

Rubin, R. H., Simpson, J. P., Lord, S. D., et al. 1994, ApJ, 420, 772

Sandstrom, K., Krause, O., Linz, H., et al. 2010, A&A, 518, 59

Smith, J. D. T., Armus, L., Dale, D. A., et al. 2007a, PASP, 119, 1133

Smith, J. D. T., Draine, B. T., Dale, D. A., et al. 2007b, ApJ, 656, 770

Sofia, U. J., Lauroesch, J. T., Meyer, D. M., & Cartledge, S. I. B. 2004, ApJ, 605, 272

Tielens, A. G. G. M., & Hollenbach, D. J. 1985, ApJ, 291, 722

Watson, W. D. 1972, ApJ, 176, 103

Weingartner, J. C., & Draine, B. T. 2001, ApJS, 134, 263

Willick, J. A., Courteau, S., Faber, S. M., et al. 1997, ApJS, 109, 333

Wolfire, M. G., Hollenbach, D. J., McKee, C. F., Tielens, A. G. G. M., & Bakes, E. L. O. 1995, ApJ, 443, 152